Acta Pharmaceutica Sinica B 2025;15(11):5945−5965

Chinese Pharmaceutical Association
Institute of Materia Medica, Chinese Academy of Medical Sciences

Acta Pharmaceutica Sinica B

www.elsevier.com/locate/apsb
www.sciencedirect.com

ORIGINAL ARTICLE

Pulmonary surfactant-biomimetic membranized coacervate injection for acute respiratory distress syndrome therapy

Wei Chen[a], Qi Xie[a], Zhanhao Zhou[b], Jia Kang[a], Yuan Gao[a], Haoyu Zhang[a], Samira Batur[a], Chuansheng Fu[a], Yunyun Li[b], Conglian Yang[a], Li Kong[a,c], Zhiping Zhang[a,c,*]

[a]*Tongji School of Pharmacy, Huazhong University of Science and Technology, Wuhan 430030, China*
[b]*Liyuan Hospital, Tongji Medical College, Huazhong University of Science and Technology, Wuhan 430030, China*
[c]*Hubei Engineering Research Centre for Novel Drug Delivery System, Huazhong University of Science and Technology, Wuhan 430030, China*

Received 24 January 2025; received in revised form 9 April 2025; accepted 12 May 2025

KEY WORDS

Coacervate;
Microdroplets;
Pulmonary surfactant;
Acute respiratory distress syndrome;
Inflammation;
Liposomes;
Dexamethasone sodium phosphate;
Macrophages

Abstract Acute respiratory distress syndrome (ARDS) is the leading cause of respiratory failure with high morbidity and mortality. Pulmonary surfactant (PS)-based complementary therapies have exhibited potential for ARDS healing and applied as an adjunctive therapy strategy. Coacervate (Coac) has the characteristics of softness, deformability and excellent molecular enrichment properties, and has attracted extensive attention in the biomedical field. Here PS and coacervate were combined for the potential ARDS treatment. The Coac, fabricated from polyallylamine hydrochloride (PAH) and adenosine triphosphate (ATP) by simple mixing, exhibited soft droplet property and high enrichment for dexamethasone sodium phosphate (DSP). To avoid the fusion effect of membraneless coacervate and endow it with biological functions of PS, liposomes with PS-biomimetic lipid components (PS-lipo) were further introduced to construct PS-biomimetic membranized coacervate (DSP@PS-Coac). The DSP@PS-Coac demonstrated high lung targeting effect and significant penetration efficiency after intravenous injection. Furthermore, PS-lipo replenished the endogenous PS pool and facilitated the distribution of DSP in inflammatory cells in the lung. In the ARDS mouse model, PS-Coac and DSP exerted synergetic anti-inflammatory functions, *via* reducing the recruitment of inflammatory neutrophils and modulating macrophages into anti-inflammatory phenotype. The overall results confirmed that DSP@PS-Coac may provide a promising delivery option for the treatment of ARDS.

*Corresponding author.
E-mail address: zhipingzhang@mail.hust.edu.cn (Zhiping Zhang).

Peer review under the responsibility of Chinese Pharmaceutical Association and Institute of Materia Medica, Chinese Academy of Medical Sciences.

https://doi.org/10.1016/j.apsb.2025.08.025

1. Introduction

Acute respiratory distress syndrome (ARDS) represents a clinical entity characterized by widespread pulmonary inflammation and edema, which typically leads to acute respiratory failure[1]. The etiological factors of ARDS are multifaceted and can be triggered by a variety of direct/indirect, intrapulmonary/extrapulmonary, and infectious/non-infectious agents[2]. Currently, the treatment for ARDS is still extremely challenging, with a mortality rate over 40%[3]. Current clinical treatments for ARDS primarily rely on lung-protective ventilation and fluid management, while drug-based therapies still require further development. Dexamethasone sodium phosphate (DSP), a glucocorticoid, is widely used as an anti-inflammatory agent in clinical practice and demonstrates significant therapeutic promise for the management of ARDS[4]. DSP can inhibit multiple inflammatory signaling pathways, modulate macrophages into an anti-inflammatory phenotype, and reduce the secretion of inflammatory factors[5]. However, the poor targeting of DSP in the body leads to serious side effects[6,7], which can cause adverse actions in multiple organs and systems[8], including neutrophilia in the blood system, osteoporosis, hyperglycemia, peptic ulcer or perforation, pancreatitis, and gastrointestinal bleeding. Currently, a series of drug delivery carriers encapsulating DSP or dexamethasone, including liposomes, nanoparticles, vesicles, lipid-vesicle fusion systems, cell membrane-liposome fusion systems, and vesicle-nanoparticle fusion systems, have been theoretically demonstrated to possess potential for improving ARDS treatment[7,9,10]. However, due to limitations such as complexities in preparation technology and challenges in clinical trials, no related product has been approved for clinical use to date. Current clinical treatments for ARDS primarily rely on lung-protective ventilation and fluid management[11]. Consequently, the development of novel DSP drug delivery systems is crucial for the treatment of ARDS.

Coacervate is a kind of liquid droplet with a uniform spherical structure through the liquid−liquid phase separation (LLPS) process, and the driven forces mainly depend on various non-covalent interactions such as electrostatic interactions, hydrogen bond interactions, and π−π interactions. A large number of studies have demonstrated that coacervates are the basis for the formation of membraneless compartments within cells[12,13]. In the field of synthetic biology, artificial organelles and cells with complex structures and diverse functions are being constructed *in vitro* by means of coacervate microdroplets[14,15], which has profound significance for understanding cellular functions, disease pathology, and the origin of life[16,17]. In recent years, coacervates have attracted widespread attention due to their unique advantages[18,19]. Therapeutic agents can be spontaneously enriched in coacervates through non-covalent interactions, which enables efficient loading of diverse therapeutic agents, including small molecules with different physicochemical properties, and biomacromolecules such as nucleic acids and proteins[20]. Meanwhile, coacervates are usually formed by LLPS in an aqueous environment without organic solvents during the drug loading process, which can effectively retain the activity of drugs[21]. Due to their unique drug-carrying capacity, soft and permeable properties[22], coacervate droplets are potentially feasible to be used as DSP delivery carriers and can effectively penetrate into the alveoli by emulating the physical properties of natural neutrophils. However, the membraneless characteristic of coacervate droplets makes them vulnerable to external environmental conditions, which usually leads to structural coalescence or destruction[23,24]. In addition, coacervate droplets typically lack lung-targeting properties, which also limits their application in pulmonary therapy. Consequently, additional stabilization of coacervate droplets is essential to withstand the complex delivery environment *in vivo* and to ensure their efficient delivery to lung lesion sites.

Pulmonary surfactant (PS) is a fundamental substance for maintaining the normal structure and function of the lungs, and is mainly synthesized by type II alveolar epithelial cells (ATIIs). PS is mainly composed of about 90 wt% lipids and 10 wt% surfactant-associated proteins (SP). The most abundant component of PS is saturated phosphatidyl dipalmitoyl phosphatidylcholine (DPPC) (∼40 wt%), followed by anionic lipid component represented by phosphatidylglycerol (PG) (7−15 wt%)[25]. During the development of ARDS, the PS barrier is severely disrupted, including the decrease in its production and secretion (mainly PC and PG), inactivation and mutation, and leakage of PS components[26,27]. Abnormal surfactant function leads to alveolar collapse, gas exchange disorders, and respiratory failure, which mainly contributes to mortality in ARDS. Therefore, exogenous PS therapy provides a new option for ARDS treatment. In clinical applications, complementary therapy with exogenous PS significantly improved survival in premature infants with ARDS[28,29]. Firstly, administering exogenous PS can effectively replenish the endogenous PS pool *in vivo*, restoring PS function and preventing alveolar collapse. In addition, PS components (mainly PC and PG) can exert innate immunomodulatory functions to protect alveoli against exogenous pathogens and particulate[30]. Inspired by this, drug carriers based on the main phospholipid components of PS for the treatment of pulmonary inflammatory diseases have been gradually explored[31,32]. Owing to the superior surface diffusion properties of PS, it can significantly enhance the distribution of drugs across the epithelial lining of the entire respiratory tract[33,34], thus achieving better therapeutic effects. During the respiratory cycle, about half of the exogenous PS components are reused through the recycling mechanism of ATIIs, while the other half is phagocytosed and degraded by alveolar macrophages (AMs)[35]. The natural recycling pathway of PS can facilitate further drug diffusion along the lung surface and target to lung epithelial cells and macrophages[36−38]. In light of the properties and functions of PS, their modification on the surface of coacervate droplets as components targeting lung cells has the potential to enhance the stability of coacervate droplets and facilitate their pulmonary drug delivery[39].

To acquire a stable carrier appropriate for pulmonary drug delivery, we employed PS as a functional membrane stabilizer to

modify the drug-containing coacervate droplets. Polyallylamine hydrochloride (PAH) exhibits good biocompatibility and has been widely used to construct various drug delivery systems (nanoparticles, hydrogels, microspheres, etc.) for the treatment of multiple diseases[40−44]. Moreover, as a cationic polymer, it has the capacity to form coacervates through electrostatic interactions with negatively charged substances (polyacrylic acid, poly(uridylic acid), etc.)[45]. Therefore, the coacervate microdroplets (Coac) were first prepared by PAH and adenosine triphosphate (ATP). Owing to the inherent molecular enrichment properties of the Coac, the anti-inflammatory drug DSP could be spontaneously and efficiently loaded into Coac (DSP@Coac). Next, we constructed biomimetic liposomes (PS-lipo) composed of the main phospholipid components of PS (DPPC, DSPG, and DOPE-PEG_{2000}), and then modified them on the surface of Coac to construct PS-biomimetic membranized Coac (PS-Coac) to avoid the fusion effect of membraneless Coac and endow it with biological functions of PS. As expected, PS-Coac exhibited excellent long-term stability as well as high drug encapsulation efficiency for various molecules (including small molecules, biomacromolecules, and nanoparticles), as well as drug DSP (DSP@PS-Coac). Similar to the soft and deformable neutrophils, DSP@PS-Coac has the potential to penetrate the interstitial space of inflamed tissues and showed preferable accumulation in the lungs after intravenous injection. Moreover, DSP@PS-Coac could be phagocytosed by macrophages and alveolar epithelial cells, releasing drugs in response to the acidic inflammatory microenvironment, which further exerted the synergetic anti-inflammatory functions of PS-Coac and DSP. In the ARDS mouse model, DSP@PS-Coac significantly reduced the recruitment of inflammatory neutrophils in the lungs and exerted multiple anti-inflammatory effects, including the inhibition of cytokine storm, the relief of pulmonary vascular leakage, and the alleviation of oxidative stress (Scheme 1). In conclusion, this novel PS biomimetic membranized coacervate microdroplet-based drug delivery system integrated the triple combinational functions of coacervate microdroplets, drug and PS, providing an effective treatment approach for ARDS.

2. Materials and methods

2.1. Materials and reagents

Poly (allylamine hydrochloride) (PAH, Mw: ∼15,000) was purchased from Sigma−Aldrich (USA). Adenosine triphosphate (ATP) was brought from Macklin (Shanghai, China). 1,2-Dipalmitoyl-*sn*-glycero-3-phosphorylcholine (DPPC) was provided with Ruixi Biological Technology (Xi'an, China). 1,2-Distearoyl-*sn*-glycero-3-phospho-(1′-rac-glycerol) (DSPG) and 1,2-distearoyl-*sn*-glycero-3-phosphoethanolamine-*N*-[methoxy(polyethylene glycol)-2000] (DOPE-PEG_{2000}) were obtained from AVT Pharmaceutical Technology (Shanghai, China). Lipopolysaccharide (LPS, L2630) was purchased from Sigma−Aldrich (USA). Dexamethasone 21-phosphate disodium salt (DSP) was obtained from Aladdin (Shanghai, China). 4,6-Diamidino-2-phenylindole (DAPI), 1,1′-dioctadecyl-3,3,3′,3′-tetramethylindocarbocyanine perchlorate (DiI), 3,3′-dioctadecyloxacarbocyanine perchlorate (DiO), 1,1′-dioctadecyl-3,3,3′,3′-tetramethylindodicarbocyanine (DiD), penicillin−streptomycin (100 ×), trypsin, 1-ethyl-3-[3-(dimethylamino)propyl]-methylthiazolyldiphenyl-tetrazolium bromide (MTT), and 2′,7′-dichlorodihydrofluorescein diacetate (DCFH-DA) were obtained from Beyotime Biotechnology (Shanghai, China). Fluorescein 5-isothiocyanate (FITC), methylene blue, coumarin-6 (C6), rhodamine B (R-B), and indocyanine green (ICG) were brought from Aladdin (Shanghai, China). Doxorubicin hydrochloride was ordered from Beijing Huafeng United Technology (Wenzhou, China). FITC-bovine serum albumin (FITC-BSA) and tetramethylrhodamine isothiocyanate-bovine serum albumin (TRITC-BSA) were brought from Solarbio Science & Technology (Beijing, China). Cytometric bead array (CBA) cytokines assay kit was purchased from BD Biosciences (NJ, USA). The assay kit of lactate dehydrogenase (LDH) was purchased from Jiancheng Bioengineering Institute (Nanjing, China). Antibodies (FITC-conjugated anti-CD11b, PE-conjugated anti-Ly6G, PerCP-Cy5.5-conjugated anti-CD45, APC-conjugated anti-F4/80 and FITC-conjugated anti-F4/80 antibodies) for flow cytometry analysis were obtained from Biolegend (CA, USA). Fetal bovine serum (FBS) was obtained from PAN Biotechnology (China). DMEM medium was purchased from Gibco (CA, USA).

2.2. Cell lines and animals

Murine macrophage cell line (RAW 264.7), human umbilical vein endothelial cell line (HUVEC) and murine lung epithelial-12 cell line (MLE-12) were purchased from the Cell Bank of Chinese Academy of Science (China). HUVEC cells and MLE-12 cells were cultured in DMEM medium supplemented with 10% fetal bovine serum and 1% penicillium−streptomycin (*v*/*v*). RAW264.7 cells were cultured in DMEM medium supplemented with 10% fetal bovine serum unless required for specific experiments. The incubator environment was maintained at 37 °C with 5% CO_2. C57BL/6 mice (Male, 8−10 weeks) were purchased from the Laboratory Animal Resources of Huazhong University of Science and Technology (HUST). All animals were fed under specific pathogen-free (SPF) environment, following the guidelines of Laboratory Animals Ethics of HUST. All animal experiments were approved by the Institutional Animal Care and Use Committee of HUST ([2024] IACUC Number 4239).

2.3. Preparation and characterization of PAH/ATP coacervate microdroplets (Coac)

PAH/ATP coacervate microdroplets were prepared by mixing PAH and ATP in saline solution (pH 7.0) at different mass ratios, and the system changed from a clear solution to a milky-white turbid solution. Typically, a positively charged PAH/ATP coacervate microdroplets suspension (3 mg/mL) can be obtained by mixing the same volume of 1 mg/mL PAH solution with 5 mg/mL ATP solution and aging for 30 min at room temperature (25 °C).

2.4. The phase diagram of transmittance

The phase diagram was mapped by measuring the transmittance of coacervate microdroplets formed with a mass ratio of PAH and ATP ranging from 1:100 to 100:1. The concentrations of the two component solutions ranged from 0.1 mg/mL to 10 mg/mL. Specifically, we used an automatic microplate reader (Multiskan

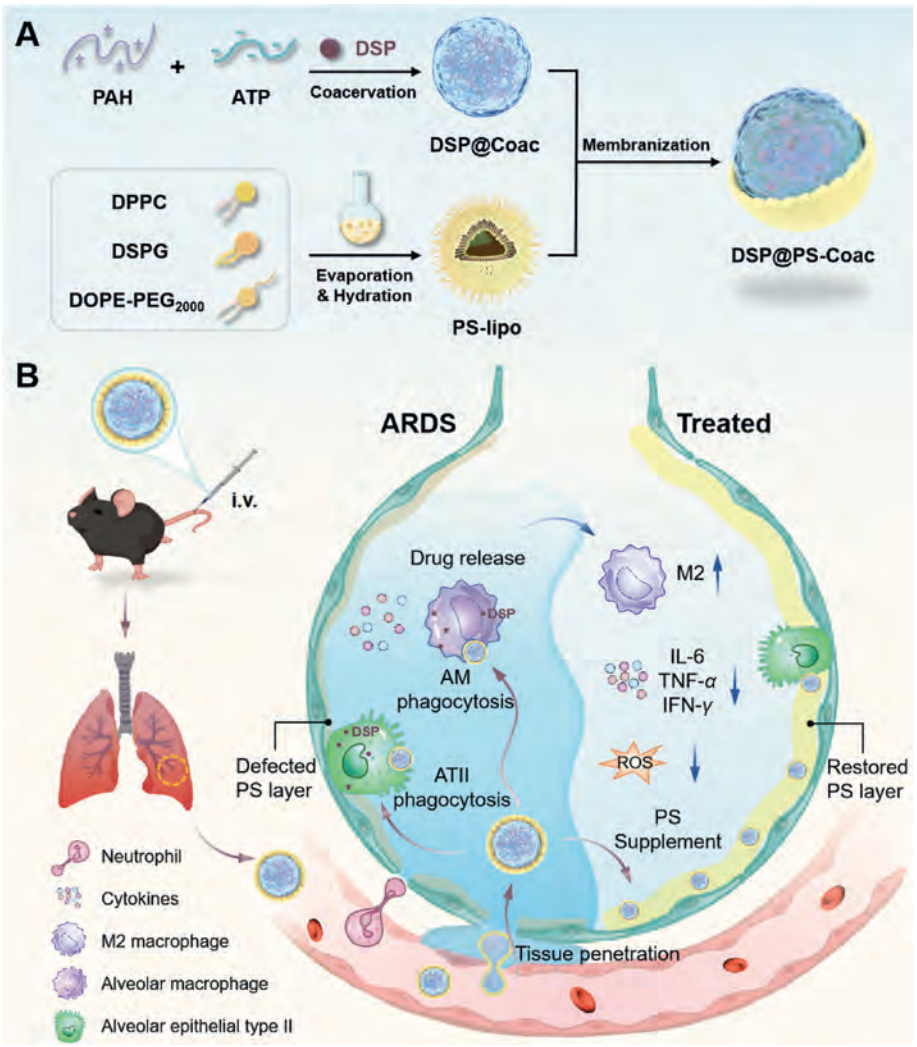

Scheme 1 Schematic representation of the preparation of DSP@PS-Coac and the application in the ARDS treatment. (A) DSP@PS-Coac was developed by modifying the surface of dexamethasone sodium phosphate-carrying coacervate microdroplets (DSP@Coac) with pulmonary surfactant-biomimetic liposomes (PS-lipo). (B) After intravenous injection, DSP@PS-Coac could target the inflamed lung. Based on its soft microdroplet properties and PS modification, DSP@PS-Coac could penetrate the interstitial space of lung tissue and the biological barrier on the lung surface, replenish the endogenous PS pool, and be phagocytosed by AMs and ATIIs. The intracellularly released DSP could play an effective anti-inflammatory role in the treatment of ARDS.

Mk3, Thermo Fisher, USA) to measure the absorbance (A) at 420 nm to calculate the transmittance (T). The transmittance was normalized (T_{norm}) by its maximum (T_{max}) and minimum (T_{min}) values. All samples were prepared and measured at room temperature (25 °C). The transmittance (T_{norm}) was calculated according to Eq. (1):

$$T\,(\%) = 1/10^{A} \times 100$$

$$T_{norm} = (T - T_{min}) / (T_{max} - T_{min}) \quad (1)$$

2.5. *The particle size and zeta potential of Coac*

The prepared coacervate microdroplets were diluted to an appropriate concentration and dispersed in a colorimetric dish. The hydrodynamic diameter and zeta potential of Coac were measured by the dynamic light scattering (DLS) detector (Zeta Plus 90, Brookhaven, USA) at 25 °C.

2.6. *Fluorescence recovery after photobleaching (FRAP) experiments*

The doxorubicin hydrochloride (DOX) with spontaneous red fluorescence was used as a model hydrophilic molecule and then loaded into Coac. FRAP experiments were performed on the Nikon AX confocal laser scanning microscope (CLSM) with 100 × Oil DIC N2 immersion objective. The emission signals were acquired in the range of 570−580 nm. Images were recorded in bidirectional scanning mode. Before photobleaching, 3 frames of images (1 frame per second) were taken at normal laser intensity. A 2.0 μm × 2.0 μm rectangular region of interest (ROI_1) inside the Coac was selected for photobleaching at maximum ultra-strong laser intensity, while another region of equal size was selected as a control (ROI_2). The laser was then switched back to

normal intensity and the image recovery process was recorded for 60 s.

2.7. Molecular enrichment properties of Coac

DAPI, FITC, methylene blue and DOX were chosen as representative hydrophilic molecules, C6 and DiD as representative hydrophobic molecules, FITC-BSA as representative of biological macromolecules, as well as poly(lactic-*co*-glycolic acid) nanoparticles (FITC-PLGA NPs) as representative of nanoparticles to investigate the ability of the Coac to enrich guest molecules with different physicochemical properties. Generally, 1 mg/mL saline solutions of DAPI, FITC, methylene blue, DOX, C6, DiD, FITC-BSA and FITC-PLGA NPs were prepared in advance. Then 500 μL of Coac was mixed with 1 μL of each of the above fluorescent molecule solutions. The mixtures were incubated for 30 min and then loaded into homemade confocal petri dishes and left for 10 min for CLSM observation.

2.8. Preparation of pulmonary surfactant-membranized Coac (PS-Coac)

PS-biomimetic liposomes (PS-lipo) were prepared utilizing the thin-film hydration method. Initially, DPPC and DOPE-PEG_{2000} were dissolved in chloroform solution, DSPG was dissolved in a mixture of chloroform and methanol (1:1, *v*/*v*), and the above solutions were homogeneously mixed at a certain molar ratio (DPPC: DSPG: DOPE-PEG_{2000} = 5:5:1), and 0.1% DiI fluorescent probe was added for CLSM observation. Subsequently, it was transferred to a round-bottomed flask and vaporized by the rotary evaporator at 60 °C for 30 min to form a homogeneous film. An appropriate volume of saline was then added for sonication and dispersion for 5 min to allow sufficient shedding of lipid film. Finally, the suspension was hydrated and incubated at 60 °C for 30 min, and then PS-lipo was obtained.

PS-Coac was prepared *via* positively charged coacervate microdroplets mixed with negatively charged PS-lipo. Typically, the PAH/ATP coacervate needed to be prepared in advance in saline solution and was incubated for 30 min. Subsequently, PS-lipo was added to the PAH/ATP coacervate microdroplet suspension to achieve a final weight ratio of 10% (PS-lipo: coacervate, *w*/*w*). After incubation for 30 min at room temperature (25 °C), a suspension of PS-Coac was obtained.

2.9. Size control behavior of membranized Coac via PS-lipo

Coac and PS-Coac were prepared separately and their time-dependent size variations were monitored by flow cytometry (FCM) at an interval of 5 min for 30 min. The dimensions of the samples after 30 min were observed by CLSM.

In order to adjust the size of PS-Coac by controlling the addition time of PS-lipo, the Coac was prepared as per the above method. Subsequently, the Coac was incubated at room temperature for 5, 15 and 30 min before the addition of PS-lipo. After 30 min of membranization, the size of PS-Coac was observed by CLSM and the size distribution was quantified with Image J.

2.10. Stability of Coac and PS-Coac

The salt and pH stability of Coac and PS-Coac were investigated by preparing Coac and PS-Coac at different salt concentrations and different pH values. Specifically, to examine their salt stability, we examined the turbidity values of Coac and PS-Coac in 50, 100, 200, 300, 400, 500, 600, 700, 800, 900 and 1000 mmol/L NaCl solutions, respectively. To examine their pH stability, the Coac and PS-Coac suspensions were adjusted to the pH of 1−14 range with HCl (1 mol/L) or NaOH (1 mol/L). The same volume of saline was used as a control (A_{blank}). The absorbance at 600 nm (A_{Coac}) of the above systems was detected by an automatic microplate reader and the corresponding turbidity was calculated. Unless otherwise stated, all assays were performed at room temperature and three parallel repeats were set up. The turbidity was calculated according to Eq. (2) [22]:

$$A_{600} = A_{Coac} - A_{blank}$$

$$\text{Turbidity } (\%) = 100 - 100 \times (100^{-A600}) \quad (2)$$

2.11. Drug loading and in vitro release of PS-Coac

Drug loading efficiency assay: to quantify the drug-carrying efficiency of DSP in PS-Coac, the DSP solution was first mixed thoroughly with PAH solution. Then the ATP solution was added and mixed thoroughly with it and incubated for 30 min. Subsequently, it was encapsulated by adding PS-lipo as described above and incubated again for 30 min to obtain DSP@PS-Coac. The supernatant was collected after centrifugation, and the content of DSP was detected indirectly by using high-performance liquid chromatography (HPLC).

In vitro drug release profile: the *in vitro* release profiles of DSP within different pH environments were determined by dialysis and measured by HPLC. In brief, 2 mL of DSP@PS-Coac (molecular weight cutoff, 3.5 kDa) was added into the dialysis bag, and the external phase was 20 mL of saline at different pH (pH 7.4, 6.5 and 5.5, respectively). The samples were incubated in a thermostatic shaker (THZ-C, Taicang Huada Experimental Instrument Technology, China) at 37 °C with the speed set to 100 rpm. 3 mL of released medium was collected for HPLC at preset time points 0, 1, 2, 4, 6, 8, 12, 24, 36 and 48 h. The remaining external phase medium was discarded, while 20 mL of fresh saline was added at each preset time point. Finally, we freeze-dried the released medium and resuspended it with 300 μL saline, and collected the supernatant after centrifugation. The DSP content was determined by HPLC and the cumulative drug release rate was calculated. HPLC conditions were set as follows: the column was Kromasil 100 - 5 C18 column (250 mm × 4.6 mm, 5 μm); the column temperature was 20 °C; the mobile phase was 0.05% trifluoroacetic acid aqueous solution/acetonitrile (0−10 min, from 20/80 to 60/40); the flow rate of the mobile phase was at 1.0 mL/min and the UV detection wavelength was at 240 nm.

2.12. Hemolysis assay

Firstly, fresh blood from healthy C57BL/6 mice anticoagulated with sodium citrate was collected and centrifuged at 400×*g* for 10 min. The red blood cells were resuspended in saline and washed until the supernatant was clarified. Subsequently, the collected red blood cells were mixed with Coac and PS-Coac solutions containing different concentrations (0.001, 0.01, 0.1, 1 and 3 mg/mL). At the same time, ultrapure water and physiological saline were added to the red blood cells as positive and negative controls. After incubating in a constant temperature

shaker at 37 °C for 3 h, collected the supernatant by centrifugation. The supernatant was transferred into a 96-well plate and the absorbance at 542 nm was measured by an automatic microplate reader. The hemolysis rate was calculated according to Eq. (3) [46]:

$$\text{Hemoglobin release (\%)} = (A_{\text{sample}} - A_{\text{saline}})/(A_{\text{water}} - A_{\text{saline}}) \times 100 \quad (3)$$

2.13. Investigation of cellular uptake of Coac and PS-Coac

RAW 264.7 cells were selected to represent alveolar macrophages, and MLE-12 were selected to represent lung structural cells to examine their uptake behavior. First, RAW 264.7 and MLE-12 cells were inoculated in 12-well plates, and the inflammation was induced by adding 100 ng/mL lipopolysaccharide (LPS). When the cells grew to a suitable density, the medium was discarded and the medium containing 25 μg/mL DiI@Coac (or DiI-DSP@Coac) or DiI@PS-Coac (or DiI-DSP@PS-Coac) was added for further co-incubation. After the incubation, the medium was discarded and the cells were gently washed 2−3 times with saline. The cells were fixed by 1 mL 4% paraformaldehyde and then washed 2−3 times with saline. Subsequently, the nuclei were stained by 1 μg/mL DAPI, and cellular uptake was observed by CLSM. For quantitative analysis, cells were collected by centrifugation and resuspended in saline, followed by measuring the intracellular fluorescence intensity using flow cytometry.

2.14. In vitro oxidative stress alleviation capacity of PS-Coac under inflammatory conditions

Intracellular inflammation mediated reactive oxygen species (ROS) production was detected by ROS probe 2′,7′-dichlorofluorescin diacetate (DCFH-DA). Specifically, RAW264.7, MLE-12, or HUVEC cells were inoculated in 12-well plates and cultured overnight under 100 ng/mL LPS stimulation. Subsequently, free DSP (30 μg/mL), PS-Coac, and DSP@PS-Coac (equivalent DSP: 30 μg/mL) were added to the fresh medium and co-incubated for 12 h, respectively. The cells were labeled with 20 μmol/L DCFH-DA for 30 min, and the free probe was removed by washing three times. Finally, the intracellular fluorescence intensity was detected by flow cytometry.

2.15. Establishment of murine ARDS model

Male C57BL/6 mice (weighing 20−22 g) at 6−8 weeks of age were selected to construct the ARDS model by tracheal drip injection of LPS (5 mg/kg). Firstly, the mice were deeply anesthetized by intraperitoneal injection of anesthetic tribromoethanol (250 mg/kg) for 5−10 min until the mice were unresponsive to gentle pinching of the tail end. Subsequently, they were fixed vertically on the surgical plate, and the tongue was gently pulled out to the right using forceps to place the laryngoscope and expose the trachea. Finally, the tracheal nebulizing needle was slowly inserted into the trachea to rapidly inject LPS (5 mg/kg) into the trachea and the mice were continued to be suspended for 30 s to allow the LPS to be distributed evenly into the lungs. The mice were placed on a thermostatic electric blanket until sobering.

2.16. Investigation of the biodistribution of DSP@PS-Coac

The ARDS model mice were induced as the method described above. The ARDS mice were divided into three groups and injected intravenously with free ICG, ICG-loaded Coac (ICG@Coac), and ICG-loaded PS-Coac (ICG@PS-Coac). The dose of ICG was 0.75 mg/kg. The mice were euthanized at predetermined time intervals (1, 3, 6, 24, and 48 h) and the major organs (heart, liver, spleen, lung and kidney) were collected to assess their biodistribution. The fluorescence of each tissue and organ was scanned by an *in vivo* imaging system (IVIS) and analyzed qualitatively and quantitatively by software.

2.17. In vivo anti-inflammatory effects of DSP@PS-Coac

ARDS model mice were randomly divided into 5 groups and i.v. injected with PBS, DSP, PS-Coac, and DSP@PS-Coac (DSP: 2 mg/kg) at 4 and 24 h after LPS induction. In addition, healthy mice with an equal volume of PBS by tracheal drip were used as a control group. All mice were euthanized 24 h after the last administration and the trachea was exposed. A puncture needle was inserted into the trachea, and then the lungs were rinsed three times with 1 mL of ice-cooled hank's balanced salt solution (HBSS) to collect lung bronchoalveolar lavage fluids (BALF). The collected BALF was centrifuged at 470×*g* for 5 min, and the supernatant and cells were separated for subsequent tests.

Erythrocytes were removed by adding red blood cell lysis buffer to the cell precipitates, and the remaining cells were collected by centrifugation and resuspended in PBS. A portion of the cells was taken to detect the total cell number in BALF by cell counter. The remaining cells were blocked with CD16/32 antibodies, and then labeled with FITC-CD11b, PE-Ly6G, PerCP-Cy5.5-CD45 and APC-F4/80 antibodies for macrophages and neutrophils, and incubated for 30 min at 4 °C, protected from light. After being terminated with PBS and washed by centrifugation, the macrophage and neutrophil percentage in the BALF was analyzed by FCM.

The BALF supernatant was centrifuged at 470 × *g* for 10 min and then frozen at −20 °C. For total protein quantification, 10 μL of sample was taken and lysed at room temperature with RIPA lysis solution. Subsequently, the samples were centrifuged at 18,000 × *g* for 5 min, and the supernatant was extracted and analyzed for the total protein content of BALF using the BCA kit. In addition, the levels of pro-inflammatory cytokines (TNF-α, IL-6, and IFN-γ) in the supernatant were detected using the CBA cytokines assay kit according to the instructions.

2.18. Histological and immunofluorescence analysis of DSP@PS-Coac treated lung tissue

ARDS model mice were treated with different drugs as described above, and the lung tissues were isolated. The lung tissues were fixed with paraformaldehyde and stored at 4 °C. After paraffin embedding, H&E staining was used to observe the lung damage. The phenotype of macrophages in lung tissue was analyzed by immunofluorescence staining, in which M1 type macrophages were labeled with inducible nitric oxide synthase (iNOS) antibody and M2 type macrophages were labeled with Arginase-1 (Arg-1) antibody. Cellular antibody expression was observed by CLSM and quantified by Image J. To evaluate the infiltration of neutrophils in lung tissue, we chose myeloperoxidase (MPO) antibody

for immunofluorescence staining. The level of MPO in lung tissues was observed by CLSM and quantified by Image J. In addition, to examine the level of oxidative stress in mouse lungs, isolated mouse lung tissues were snap-frozen in liquid nitrogen for 5 min and placed at −80 °C for storage, and cryosections were prepared and stained for ROS immunofluorescence. The level of ROS in lung tissues was observed by CLSM and quantified by Image J.

2.19. Statistical analysis

All experiments were repeated at least three times. Error bars indicate the standard deviation of the independent samples in the experiment. Data were analyzed by GraphPad Prism 8.0 software. A two-tailed unpaired Student's *t*-test was used to analyze between-group differences between two sample groups. For statistical analysis of experiments with three or more groups the analysis of variance (ANOVA) was used. $*P < 0.05$, $**P < 0.01$, $***P < 0.001$ and ns: not significant.

3. Results and discussion

3.1. Preparation and characterization of PAH/ATP-based coacervate microdroplets

The coacervate microdroplets constructed in this study were formed from two components, the cationic polyallylamine hydrochloride (PAH), and the anionic adenosine triphosphate (ATP). PAH/ATP coacervate microdroplets (Coac) were prepared by directly mixing the cationic polymer PAH and anionic ATP in the saline solution, and the preparation process was illustrated in Fig. 1A. To further investigate the factors influencing the formation of Coac, we examined the formation of Coac over a range of polyelectrolyte mass concentration ratios (PAH: ATP, 1:100−100:1). The phase diagram of the two-component system was plotted by measuring the transmittance of the Coac suspensions at the absorbance of 420 nm (Fig. 1B). The results indicated that both the concentration and the mass ratio of the two components affected the formation of Coac, with the polymer mass ratio being a crucial factor for the formation and morphology of Coac. We measured the zeta potential of the system within the PAH:ATP mass ratio range of 0.01−2.0 (Fig. 1B, points: a−i) to identify the Coac that was closest to the charge neutrality for subsequent characterization. The results showed that the system was closest to charge neutrality with a weak positive charge when the mass ratio of PAH to ATP was 0.2 (Fig. 1C, point d). The hydrodynamic diameter of the Coac reached a maximum at this ratio as shown by dynamic light scattering (Fig. 1D). This result was further verified by optical microscopy images (Supporting Information Fig. S1). Consequently, we selected the Coac with a PAH concentration of 1 mg/mL, an ATP concentration of 5 mg/mL, and a mass ratio 0.2 for subsequent experiments. Under the optical microscopy, the Coac exhibited a bright circular droplet structure (Fig. 1E). Additionally, we also observed that adjacent droplets would gradually fuse over time, resulting in a gradual increase in droplet size (Fig. 1F and G), which was consistent with the previous report[47]. It demonstrated that the droplets formed by PAH and ATP were soft and deformable droplets rather than traditional solid microspheres. Therefore, when these microdroplets flowed through blood vessels, they could deform under the influence of the shear force in the bloodstream and pass through narrow vascular regions, thereby reducing the risk of vessel blockage caused by rigid microspheres. The liquid properties of the Coac were further investigated by fluorescence recovery after photobleaching (FRAP) experiments. We selected doxorubicin hydrochloride (DOX), a small molecule drug with spontaneous red fluorescence, as the model molecule and encapsulated it within Coac. First, by directly mixing DOX with the Coac or PAH solutions, we demonstrated that DOX stably existed in both systems without precipitation, which was attributable to the weakly acidic environment of PAH solution (Supporting Information Fig. S2). Subsequently, we carried out further observations with a confocal laser scanning microscope (CLSM). The results showed that the red fluorescence could be rapidly recovered within 1 min after quenching, proving that the interior of the DOX-loaded Coac possessed a high degree of internal fluidity (Fig. 1H and I).

An important characteristic of coacervates is their ability to effectively enrich a wide variety of guest molecules through noncovalent interactions[48,49]. To gain a deeper understanding of this property, we selected small molecule compounds, biomacromolecules, and nanoparticles as fluorescent models to examine the enrichment of different molecules within the droplets by CLSM (Fig. 2A). The results showed that all the tested molecules and nanoparticles can be effectively enriched inside Coac, including hydrophilic DAPI, slightly soluble FITC, soluble methylene blue, soluble DOX, slightly soluble C6, lipophilic DiD, soluble macromolecular protein FITC-BSA, and nanoparticles such as FITC-PLGA NPs. Meanwhile, we further investigated the ability of Coac to co-encapsulate drug molecules of different properties. Firstly, small molecule DAPI and macromolecular protein FITC-BSA were selected to examine the ability of Coac to co-load small molecules and biomacromolecules (Fig. 2B and C). Then, hydrophilic DAPI and lipophilic DiI were selected to examine the ability of Coac to co-load hydrophilic and hydrophobic molecules (Fig. 2D and E). In the sequential layer scanning and sphere stacking images, we found that both sets of fluorescent molecules inside the Coac achieved good co-localization. The above results demonstrated that the coacervate microdroplets possessed good drug loading and co-loading potential. Moreover, since coacervate microdroplets are formed by LLPS dominated by electrostatic interactions, the salt concentration in the environment has an important impact on both the formation and stability of coacervates. Therefore, we examined the turbidity change of Coac within 1 h by incubating with NaCl solutions ranging from 0 to 1000 mmol/L, to determine whether the Coac could exist stably. As shown in Fig. 2F, Coac was stable at physiological salt concentration (154 mmol/L), and it was also stable at even higher salt concentrations (500 mmol/L). The above results were further verified by observing the state of Coac at different salt concentrations under optical microscopy (Supporting Information Fig. S3). However, we found that the turbidity of the system gradually decreased with time during 60 min. The speculated reason might be the instability caused by the fusion between droplets, which was attributed to the membraneless characteristic of coacervate microdroplets and might greatly hinder the *in vivo* application of coacervate microdroplets. In addition, the concentration of polyelectrolyte molecules is also an important factor influencing the LLPS process, and below its critical saturation concentration may lead to Coac depolymerization. Next, we examined the dilution resistance of Coac by diluting it at different

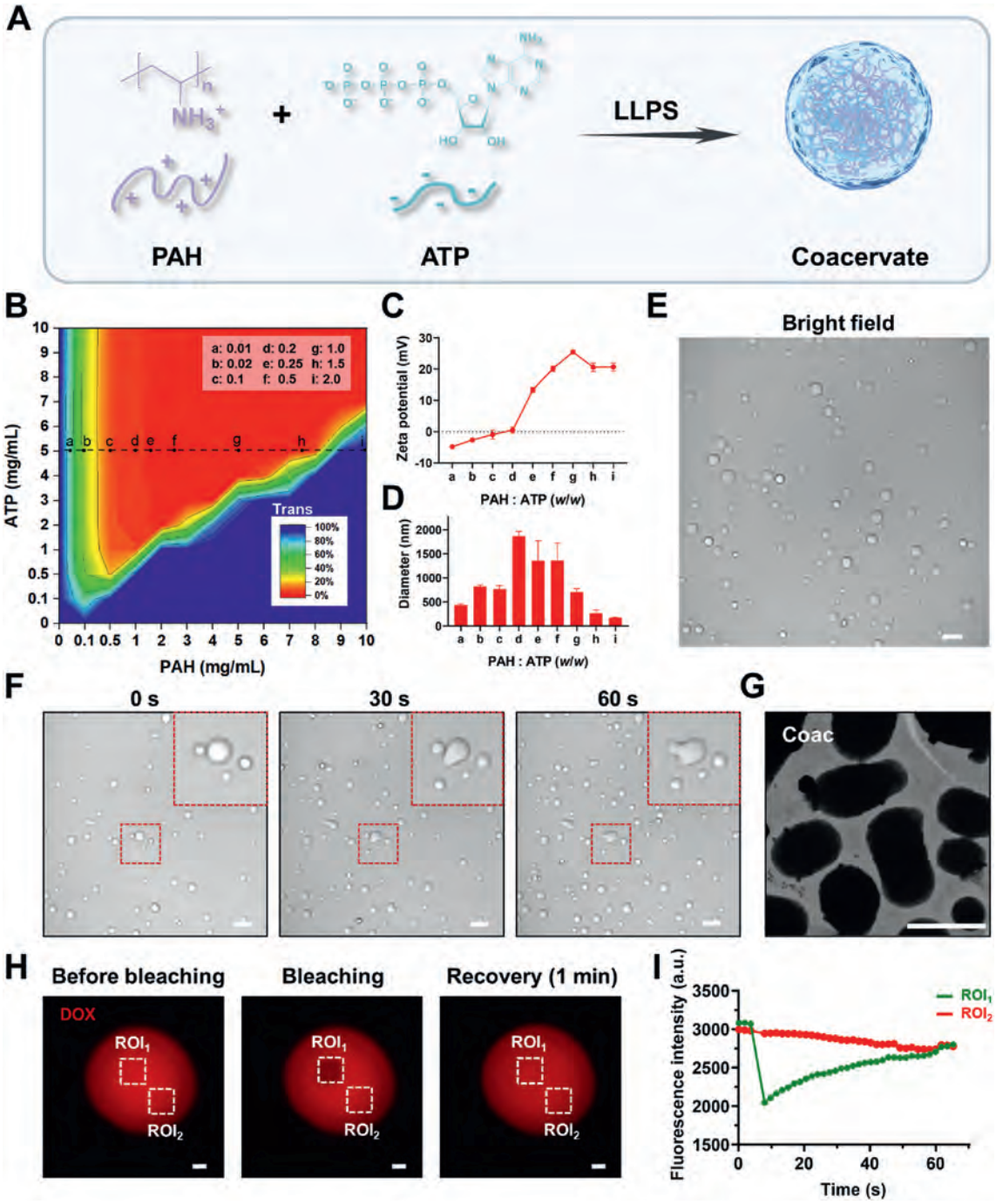

Figure 1 Construction and characterization of PAH/ATP-based coacervate microdroplets. (A) Schematic illustration of the formation of Coac *via* LLPS between PAH solution and ATP solution with opposite charges. (B) Partial phase diagram of PAH/ATP liquid−liquid phase separation based on transmittance measurements (Trans., 420 nm) recorded at different polyelectrolyte concentrations. (C) Zeta potential and (D) the average hydrodynamic diameter of Coac formed at different polyelectrolyte weight ratios (0.01−2.0, *w*/*w*). Values are expressed as mean ± SD ($n = 3$). (E) Optical microscopy image of Coac. Scale bar = 10 μm. (F) Images of Coac over time, where the fusion of Coac was shown in the red square. Scale bar = 10 μm. (G) TEM image of Coac. Scale bar = 2 μm. (H) The representative time-lapse CLSM images before (left), during (middle), and after (right) photobleaching in the FRAP experiment. ROI_1 indicated the photo-bleached area and ROI_2 indicated the control area. Scale bar = 1 μm. (I) The time-dependent change curve of the fluorescence intensity recorded within 1 min.

dilution factors and measuring the turbidity at 600 nm. The results showed that about 20% of turbidity could still be detected in the system after Coac was diluted 50 times, proving that Coac had good dilution resistance (Fig. 2G).

3.2. *Construction and evaluation of PS-Coac*

Thermodynamically, membraneless coacervates are less stable and have a tendency to grow continuously through merger or Ostwald

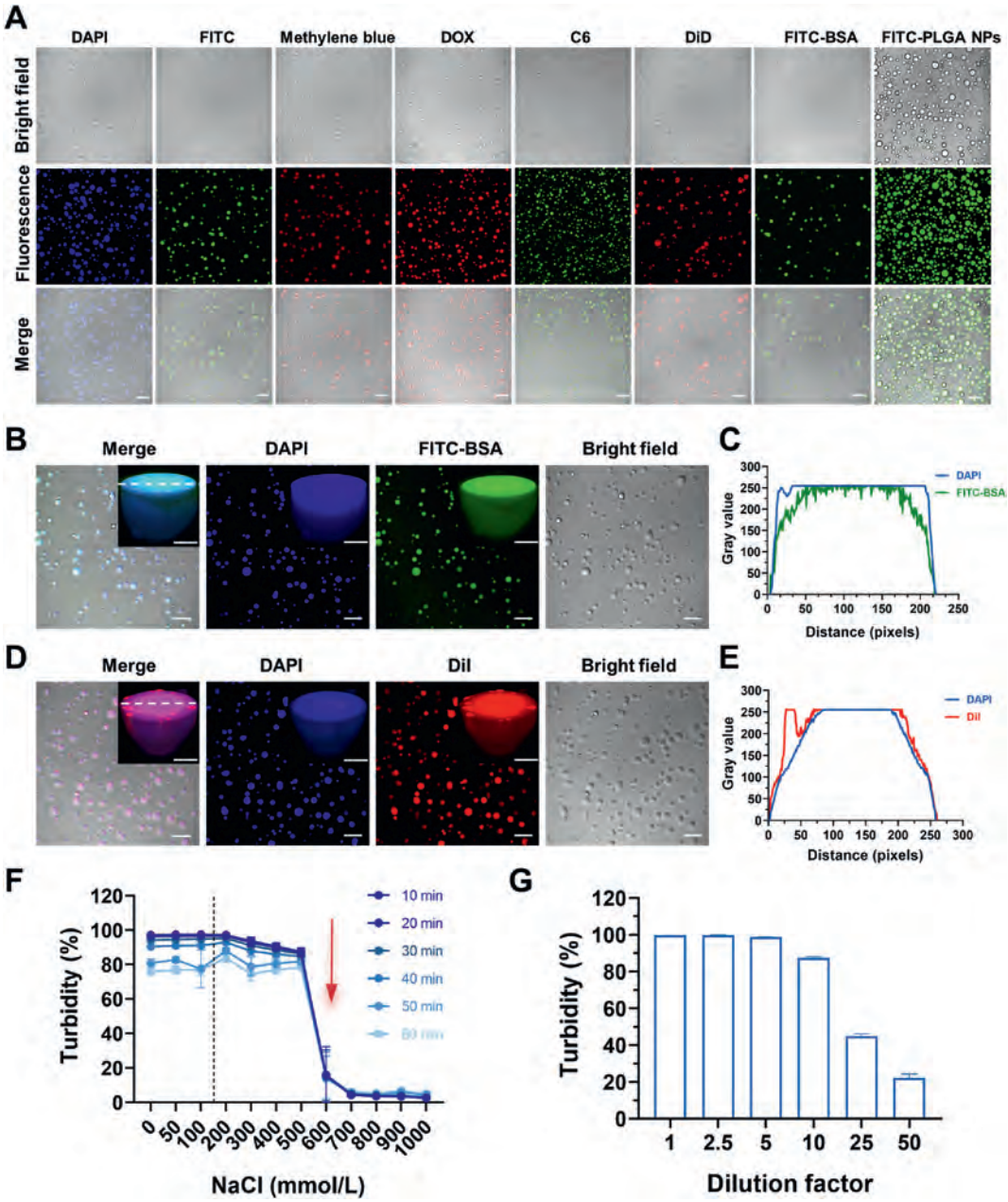

Figure 2 The enrichment capacity and stability analysis of Coac. (A) CLSM images of Coac loaded with different fluorescent molecules such as DAPI, FITC, methylene blue, adriamycin, C6, DiD, FITC-BSA and FTIC-PLGA NPs, respectively. Scale bar = 20 μm. (B) CLSM images of Coac simultaneously loaded with the small molecule DAPI and the biomacromolecule FITC-BSA. Scale bar = 20 μm. The 3D reconstructed images of a single microdroplet (upper right images). Scale bar = 5 μm. (C) The cross-sectional fluorescence quantification curve from the line drawn in Fig. 2B. (D) CLSM images of Coac loaded with both the hydrophilic molecule DAPI and the hydrophobic molecule DiI. Scale bar = 20 μm. The 3D reconstructed images of a single Coac (top right images). Scale bar = 5 μm. (E) The cross-sectional fluorescence quantification curve from the line drawn in Fig. 2D. (F) Turbidity changes of Coac in different concentrations of NaCl solutions over 1 h. The dashed line indicated the physiological salt concentration (154 mmol/L). Red arrows indicated the decrease in turbidity over the time. (G) Turbidity changes of Coac after different dilution factors. Data are represented as mean ± SD (n = 3).

maturation[50]. It has been reported that both amphiphilic molecules (fatty acids, phospholipids, etc.) and amphiphilic nano- or micro-scale objects (liposomes, cell fragments, etc.) can form complete membrane-like structures through the interfacial self-assembly function on the surface of coacervates[51]. Therefore, in order to overcome the instability of membraneless coacervate droplets and endow them with specific biological functions at the same time, thereby improving their potential for application as drug delivery carriers in living organisms, we constructed negatively charged pulmonary surfactant biomimetic liposomes (PS-lipo) based on the main phospholipid components of pulmonary surfactant (DPPC: DSPG: DOPE-PEG$_{2000}$ = 5:5:1) for Coac biomimetic

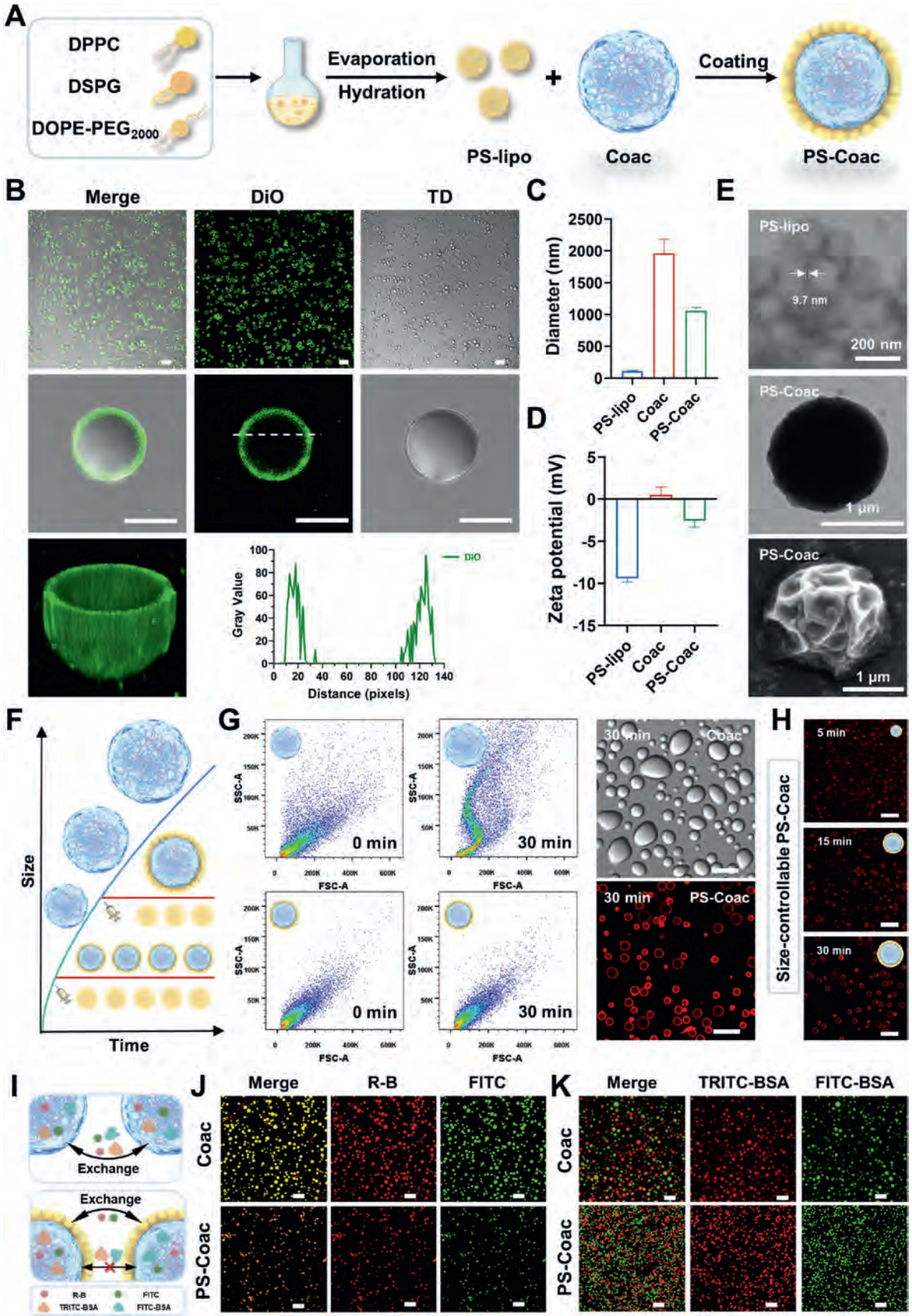
A
DPPC
DSPG
DOPE-PEG2000
Evaporation
Hydration
PS-lipo
Coac
Coating
PS-Coac
B
Merge
DiO
TD
Gray Value
Distance (pixels)
C
Diameter (nm)
PS-lipo
Coac
PS-Coac
D
Zeta potential (mV)
E
PS-lipo
9.7 nm
200 nm
PS-Coac
1 μm
F
Size
Time
G
0 min
30 min
FSC-A
SSC-A
H
30 min Coac
30 min PS-Coac
5 min
15 min
30 min
Size-controllable PS-Coac
I
Exchange
R-B
TRITC-BSA
FITC
FITC-BSA
J
Merge
R-B
FITC
Coac
PS-Coac
K
Merge
TRITC-BSA
FITC-BSA

modification (PS-Coac) (Fig. 3A). The constructed PS-lipo had the particle size of approximately 100 nm with the PDI value of less than 0.3, indicating good dispersibility and uniformity. PS-lipo exhibited good stability within 7 days (Supporting Information Fig. S4). After labeling PS-lipo with DiO and co-incubating with Coac, CLSM images clearly revealed that the green fluorescence formed a hollow circular structure on the surface of Coac (Fig. 3B). By scanning individual droplets layer by layer, we obtained 3D reconstructed image of PS-Coac. The image showed that the PS-lipo was completely dispersed across the Coac surface. Therefore, we successfully prepared PS-Coac with a membrane-like structure. After being coated with PS-lipo, the hydrodynamic size of Coac decreased, which may be attributed to the membrane-like structure making the Coac more condensed (Fig. 3C). Meanwhile, based on the negative charge of DSPG in PS-Coac, the surface charge of PS-Coac also reversed after being membrane-coated (Fig. 3D). It indicated that the modification of PS-lipo on the surface of Coac mainly depended on the interfacial self-assembly process mediated by the electrostatic interfacial interactions between them. Transmission electron microscope (TEM) images showed that the PS-lipo had a bilayer phospholipid structure (Fig. 3E, top). The PS-Coac was also characterized by TEM and scanning electron microscope (SEM), and the images showed that the surface of PS-Coac exhibited wrinkled membrane structures (Fig. 3E, middle and bottom). It was speculated that the reason might be the collapse of the surface membrane structure caused by the dehydration inside the coacervate microdroplets during the TEM and SEM sample preparation process.

To evaluate the membranization integrity of PS-lipo on Coac, we first observed macroscopically the changes of Coac and PS-Coac in glass bottles. The results showed that the PS-lipo could effectively prevent the fusion and aggregation of Coac. After 3 h, Coac gradually aggregated and fused on the sidewalls and bottom of the glass bottle, and after 30 days it could not be re-dispersed by vortexing. The sedimentation rate of PS-Coac was obviously slowed down, and it was still easy to be re-dispersed by vortexing after 30 days (Supporting Information Fig. S5). The morphology and internal fluorescent molecules of PS-Coac re-dispersed after 30 days were observed to remain stable by CLSM (Supporting Information Fig. S6). Subsequently, we used the statistical features of flow cytometry to further evaluate the effect of membrane coating. It was found that in the absence of PS-lipo, both the forward scattered light (FSC-A) and side scattered light (SSC-A) of Coac were observed to increase over time, indicating an increase in droplet size and its internal complexity (Fig. 3F, Supporting Information Figs. S7 and S8). The fusion effect could be inhibited by PS-lipo membranization, that is, the diameter of the coacervate microdroplets remained basically unchanged after the addition of PS-lipo, as shown in Fig. 3G. The CLSM images confirmed this result, in which the size of the PS-Coac was mostly within the range of 2−4 μm, while the membraneless Coac partially fused, grew and deformed to more than 10 μm after 30 min of incubation (Supporting Information Fig. S9). Based on this, we further verified the possibility of adjusting the size of PS-Coac by adding PS-lipo at different time points (*i.e.*, 5, 15 and 30 min). CLSM images showed that the median diameter of PS-Coac gradually increased from 1.2 μm to 2.9 μm (Fig. 3H and Supporting Information Fig. S10). It was demonstrated that the size of PS-Coac could be adjusted as needed by controlling the addition time of liposomes. We chose to add PS-lipo 30 min after the Coac had aged to control most of the size of most PS-Coac to around 2.9 μm for subsequent experiments. At this size, the droplets might accumulate in the lungs through passive targeting mechanisms. Furthermore, since this dimension was smaller than the diameter of most pulmonary capillaries in mice (5−10 μm), the droplets could theoretically be able to pass through the microcirculation system[52].

To investigate whether PS-Coac can be stabilized in a physiological environment, we further examined the stability of PS-Coac under different NaCl concentrations. The results demonstrated that PS-Coac maintained good salt stability compared with Coac, and no decrease in turbidity was observed within 1 h (Supporting Information Figs. S11 and S12). By subjecting the PS-Coac suspension to gradient dilution, we found that the turbidity values were greater than Coac at the same multiplicity of dilution, proving that the PS-lipo coating effectively enhanced the dilution resistance of Coac and might possess better potential for *in vivo* application (Supporting Information Fig. S13). Moreover, there was no significant difference in the size and number of Coac or PS-Coac at 4−60 °C, indicating that they could exist stably at physiological temperatures and possess good adaptability to different transportation and storage environments (Supporting Information Fig. S14). To examine the molecular barrier function of PS-lipo, we mixed two sets of Coac or PS-Coac encapsulated with different fluorescent molecules. Firstly, two types of small molecule fluorophores or macromolecular fluorophores were pre-isolated in Coac or PS-Coac respectively, and then these two populations were mixed at a volume ratio of 1:1 (Fig. 3I−K). The results showed that the PS-lipo coating had a good barrier effect on macromolecular substances, and no mixing of the two fluorescent molecules occurred in the PS-Coac group. However, small molecules could undergo material exchange between different PS-Coac, which would be beneficial for the release of small molecule drugs from PS-Coac.

Figure 3 Construction and characterizations of PS-Coac. (A) Schematic of the preparation process of PS-Coac. (B) CLSM images of PS-Coac constructed by adsorbing PS-lipo (DiO, green) onto the Coac surface. Scale bar = 20 μm. CLSM and 3D reconstructed fluorescence images of individual PS-Coac in cross section and quantitative results of green fluorescence intensity across PS-Coac. Scale bar = 5 μm. (C) Mean hydrodynamic diameters and (D) zeta potentials of PS-lipo, Coac, and PS-Coac. Data are represented as mean ± SD (n = 3). (E) TEM images of PS-lipo and PS-Coac, and SEM image of PS-Coac. (F) Schematic diagram of the fusion and growth of Coac over time and the regulation of the size of PS-Coac by adding PS-lipo at different time points. (G) The flow cytometry scatter plots of Coac and PS-Coac incubated for 0 and 30 min for FSC-A and SSC-A. Optical microscopy image of Coac and CLSM image of PS-Coac (PS-lipo labeled by DiD, red) after incubation for 30 min. Scale bar = 10 μm. (H) CLSM images of PS-Coac constructed by adding PS-lipo (DiD, red) at different time points (*i.e.*, 5, 15, 30 min). Scale bar = 10 μm. (I) Schematic representation of the barrier effect of Coac/PS-Coac on large/small molecules. (J) CLSM images of the mixture of R-B-loaded coacervate, R-B@Coac (or R-B@PS-Coac) and FITC-loaded coacervate, FITC@Coac (or FITC@PS-Coac). Scale bar = 10 μm. (K) CLSM images of the mixture of TRITC-BSA-loaded coacervate, TRITC-BSA@Coac (or TRITC-BSA@PS-Coac) and FITC-BSA-loaded coacervate, FITC-BSA@Coac (or FITC-BSA@PS-Coac). Scale bar = 10 μm.

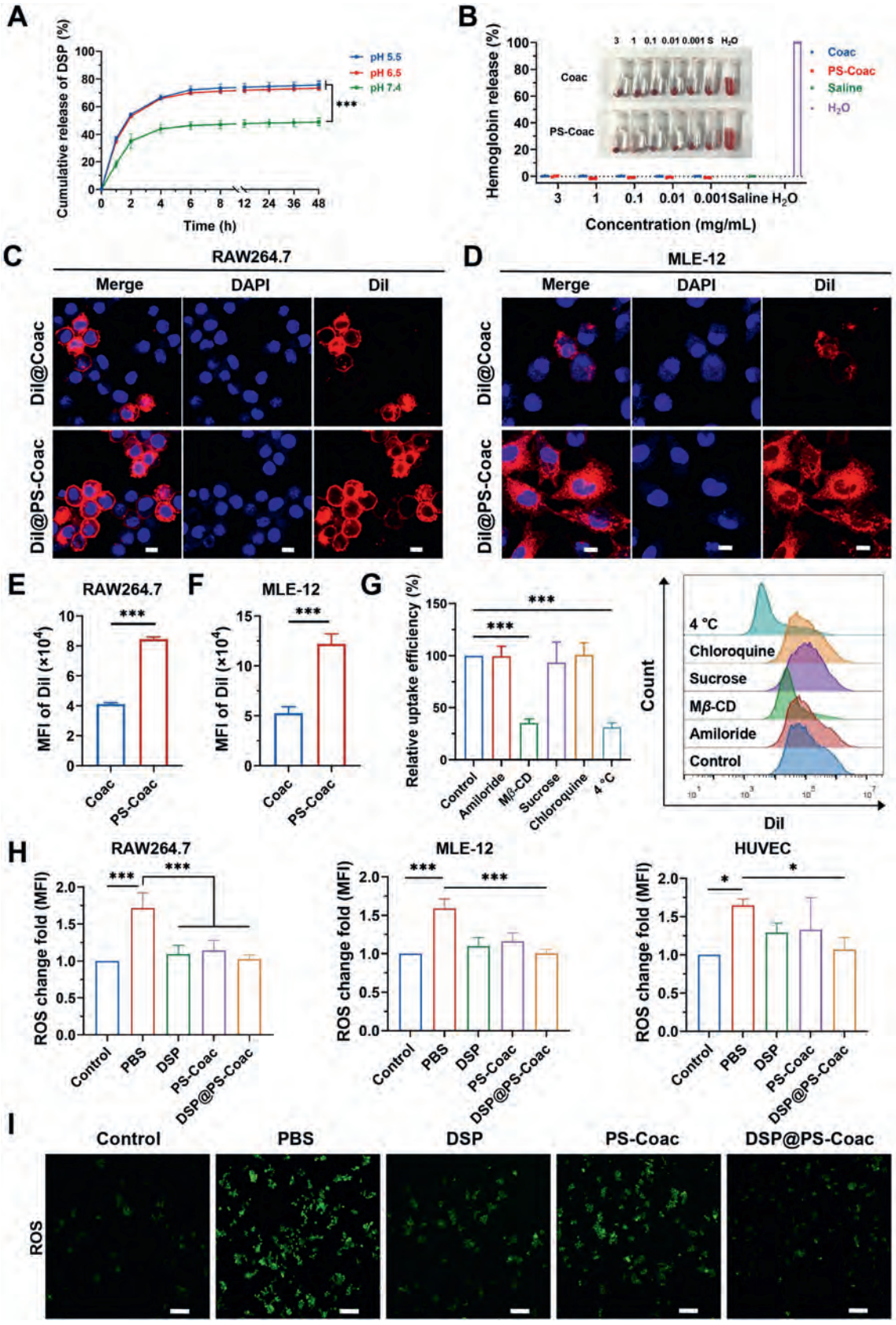
A
Cumulative release of DSP (%)
pH 5.5
pH 6.5
pH 7.4
***
Time (h)
B
Hemoglobin release (%)
3 1 0.1 0.01 0.001 S H2O
Coac
PS-Coac
Coac
PS-Coac
Saline
H2O
Concentration (mg/mL)
C
RAW264.7
Merge
DAPI
DiI
DiI@Coac
DiI@PS-Coac
D
MLE-12
Merge
DAPI
DiI
DiI@Coac
DiI@PS-Coac
E
RAW264.7
MFI of DiI (×10^4)
Coac
PS-Coac
F
MLE-12
MFI of DiI (×10^4)
Coac
PS-Coac
G
Relative uptake efficiency (%)
Control
Amiloride
MβCD
Sucrose
Chloroquine
4 °C
Count
4 °C
Chloroquine
Sucrose
MβCD
Amiloride
Control
DiI
H
RAW264.7
MLE-12
HUVEC
ROS change fold (MFI)
Control
PBS
DSP
PS-Coac
DSP@PS-Coac
I
Control
PBS
DSP
PS-Coac
DSP@PS-Coac
ROS

3.3. In vitro drug release and biocompatibility examination of PS-Coac

To evaluate the drug encapsulation efficiency (EE) of PS-Coac, we initially co-incubated the prepared Coac with the DSP solution to construct DSP-loaded Coac (DSP@Coac), and then added PS-lipo to form DSP@PS-Coac. The content of DSP was detected by high-performance liquid chromatography (HPLC), and the EE value of DSP in PS-Coac was calculated to be 77.41 ± 0.02%. Furthermore, normal saline solutions with different pH values were employed to simulate the corresponding normal physiological environment (pH 7.4), inflammatory microenvironment (pH 6.5), and lysosomal environment (pH 5.5), respectively, for examining the *in vitro* drug release behaviour of DSP@PS-Coac. As shown in the drug release curve in Fig. 4A, compared with the normal physiological environment, the drug release efficiency was obviously increased under the slightly acidic environment. Specifically, DSP was released slowly under the condition of pH 7.4, with a total release rate within 48 h of only 49.00 ± 2.78%. However, in the slightly acidic environments (pH 6.5 and 5.5), the release rate of the drug was accelerated, with 73.49 ± 1.68% and 75.78 ± 2.75% of DSP released within 48 h, respectively. Among them, the release amount of DSP under the condition of pH 5.5 was slightly higher than that under the condition of pH 6.5. It was speculated that the possible reason was that under acidic conditions, H^+ ions could penetrate the membrane barrier and enter the interior of Coac, which may cause ATP molecules to obtain partial protons, thus affecting the electrostatic interaction with positively charged PAH and leading to the slow disassembly of part of the Coac. In contrast, under physiological conditions, the small molecule drug DSP might be released through the small molecule substance exchange process mediated by the concentration difference between Coac and the external phase solution as described above. Therefore, the release rate was slower relative to the acidic environment. In summary, PS-Coac can effectively encapsulate DSP, reduce drug leakage during blood circulation, and effectively release anti-inflammatory drugs in the inflammatory microenvironment and lysosomal microenvironment, thus exerting drug efficacy.

Hemocompatibility is an important indicator for evaluating the safety of drug delivery carriers. Good hemocompatibility is a necessary condition for further application *via* the intravenous injection route in animal or clinical experiments. Consequently, we investigated whether Coac and PS-Coac caused damage to erythrocytes by *in vitro* hemolysis experiments to evaluate their biocompatibility. The results demonstrated that when the concentrations of Coac and PS-Coac were as high as 3 mg/mL, their hemolysis rates were still lower than 5%, and no obvious hemolysis phenomenon occurred (Fig. 4B). Meanwhile, the drug-loaded Coac and PS-Coac systems also showed similar results (Supporting Information Fig. S15). This indicated that the above-mentioned systems all complied with the national biosafety standards[53] and possessed good hemocompatibility.

3.4. The cellular uptake and in vitro oxidative stress alleviation capacity of PS-Coac under inflammatory conditions

Alveolar macrophages (AMs) represent the essential cells within the inflammatory activation process of ARDS. Type II pulmonary epithelial cells (ATIIs), functioning as the synthetic locus for pulmonary surfactant and as significant structural cells of alveoli, assume a crucial role in the progression of ARDS. Accordingly, RAW 264.7 cells were selected to mimic alveolar macrophages, and MLE-12 cells were chosen to represent pulmonary structural cells for the investigation of the cellular uptake of PS-Coac. Firstly, DiI@Coac and DiI@PS-Coac were incubated with RAW 264.7 and MLE-12 cells under lipopolysaccharide (LPS)-induced inflammatory conditions. Subsequently, the cellular uptake was observed *via* CLSM (Fig. 4C and D). The results showed that both RAW 264.7 cells and MLE-12 cells demonstrated higher uptake of PS-Coac than the Coac. Quantification of cellular uptake by flow cytometry revealed that PS-Coac was efficiently phagocytosed by RAW 264.7 cells and MLE-12 cells, which was consistent with the results obtained from CLSM (Fig. 4E and F). In addition, we further investigated the uptake capacity of these two types of inflammatory cells for the drug-loaded PS-Coac. The results showed that they had a stronger uptake of the drug-loaded PS-Coac than the drug-loaded Coac (Supporting Information Figs. S16 and S17). It further demonstrated that PS-Coac had a stronger ability to transport drugs into cells. To further explore the cellular uptake pathway of PS-Coac, various inhibitors including amiloride (macropinocytosis inhibitor), methyl-β-cyclodextrin (lipid raft-mediated endocytosis inhibitor), sucrose (clathrin-mediated endocytic pathway inhibitor), and chloroquine (endosomal acidification and membrane fusion inhibitor) were employed to study the uptake mechanism of cells for PS-Coac. Prior to co-incubation with DiI@PS-Coac, RAW 264.7 cells were pretreated with the aforementioned different intracellular endocytosis inhibitors, respectively. Meanwhile, a group of cells cultured at 4 °C was established to examine whether its uptake was influenced by energy. As depicted in Fig. 4G, the uptake ability of PS-Coac was inhibited to some extent under the condition of 4 °C, indicating that the endocytosis of PS-Coac was energy-dependent. Furthermore, after pretreatment with amiloride, sucrose, and chloroquine, there was no significant alteration in the cellular uptake efficiency of PS-Coac compared to that of the control group. However, following pretreatment with methyl-β-cyclodextrin, the cellular uptake rate decreased to 35.3% of the original value. All inhibitors except methyl-β-cyclodextrin failed to block the cellular uptake of PS-Coac, suggesting that the *in vitro* cellular uptake was not related to macropinocytosis, lattice proteins, and endosomal pathways, but rather to a lipid raft-mediated passive uptake mechanism based on membrane fluidity.

During inflammation progression, high levels of endogenous reactive oxygen species (ROS) (ranging from 10 to 1000 μmol/L) are generated in the inflammatory microenvironment, which can exacerbate cell damage and even lead to cell death. Reducing the

Figure 4 *In vitro* behaviour of PS-Coac. (A) *In vitro* DSP release profile of DSP@PS-Coac at different pH conditions. (B) Hemolysis rates of Coac and PS-Coac compared to water and saline. Concentrations were calculated by PAH and ATP. CLSM images of the cellular uptake behaviour in (C) RAW264.7 cells and (D) MLE-12 cells. Scale bar = 10 μm. Flow cytometry quantification results of cellular uptake behaviour in (E) RAW264.7 and (F) MLE-12 cells. (G) Effects of different endocytosis inhibitors on DiI@PS-Coac cellular uptake pathway. (H) Flow cytometry examination of the effect of DSP@PS-Coac on ROS levels in RAW264.7, MLE-12 and HUVEC cells. (I) CLSM images of ROS fluorescence in RAW264.7 cells treated with different drugs. Scale bar = 100 μm. All groups were treated with LPS except the control group. Data are expressed as mean ± SD ($n = 3$); *$P < 0.05$, ***$P < 0.001$.

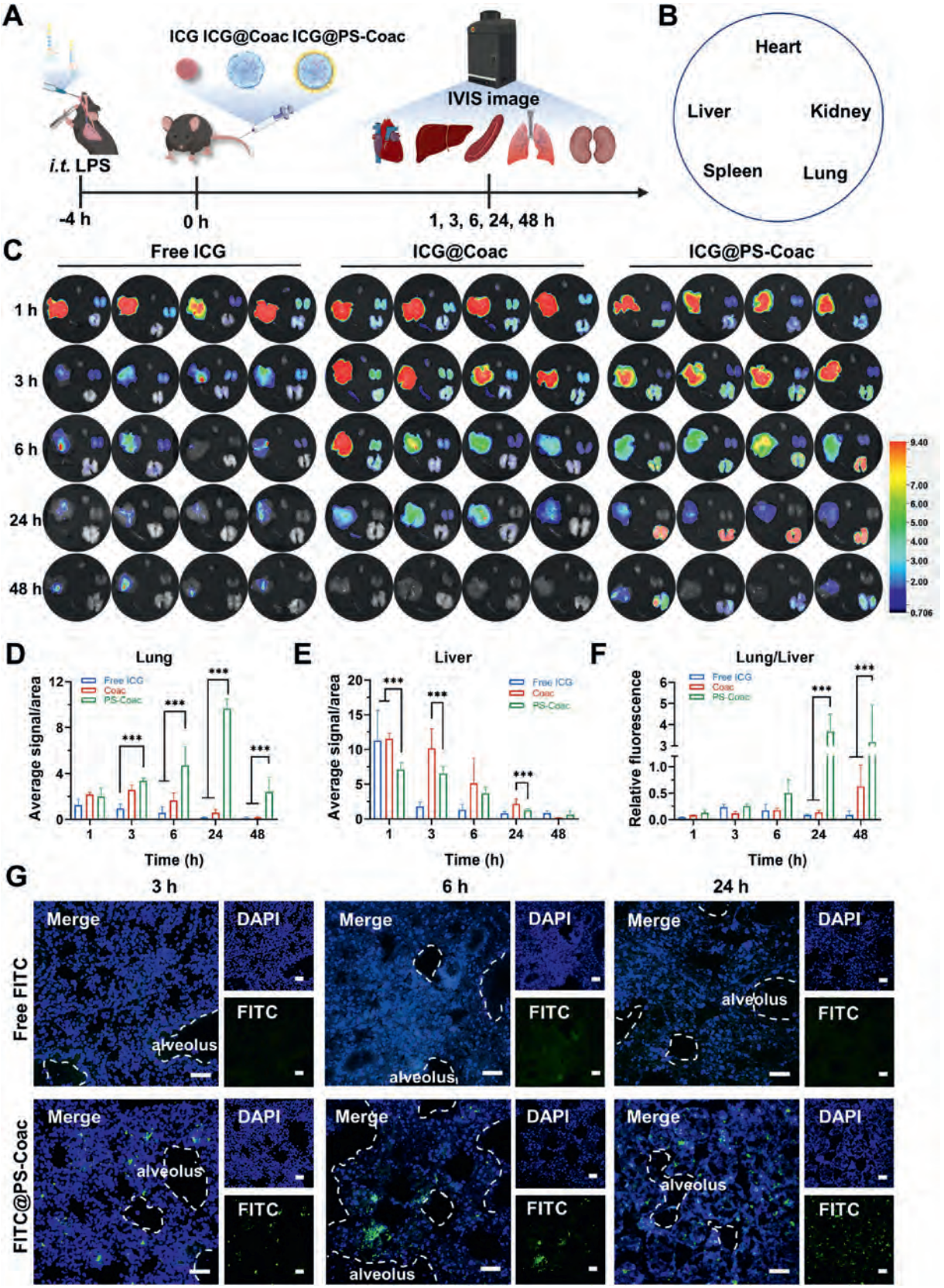
A
ICG ICG@Coac ICG@PS-Coac
IVIS image
i.t. LPS
-4 h
0 h
1, 3, 6, 24, 48 h
B
Heart
Liver
Kidney
Spleen
Lung
C
Free ICG
ICG@Coac
ICG@PS-Coac
1 h
3 h
6 h
24 h
48 h
9.40
7.00
6.00
5.00
4.00
3.00
2.00
0.706
D
Lung
Average signal/area
Free ICG
Coac
PS-Coac
Time (h)
E
Liver
Average signal/area
Time (h)
F
Lung/Liver
Relative fluorescence
Time (h)
G
3 h
6 h
24 h
Free FITC
FITCPS-Coac
Merge
DAPI
FITC
alveolus

production of ROS has thus become an effective strategy for the treatment of ARDS. Therefore, to further evaluate the potential of DSP@PS-Coac in the treatment of ARDS, we investigated the anti-inflammatory effect *in vitro* by evaluating its properties to regulate oxidative stress. We evaluated the potential of DSP@PS-Coac to alleviate inflammation-induced oxidative stress *in vitro* in LPS-induced inflammatory RAW 264.7, MLE-12, and HUVEC cell models, respectively. The above-mentioned cells were firstly stimulated with LPS for 12 h to induce oxidative stress damage, and then different formulated drugs were added to treat the cells for another 12 h. After being labeled with ROS fluorescent probes, the expression levels of ROS in each group of cells were detected by flow cytometry. The results demonstrated that the ROS production within RAW 264.7, MLE-12, and HUVEC cells was obviously increased after LPS stimulation, with the levels being 1.72 times, 1.59 times, and 1.65 times higher than those in the control group, respectively. Following the intervention of DSP@PS-Coac, the ROS levels decreased to approach normal levels, indicating that DSP@PS-Coac could effectively down-regulate the ROS levels in multiple inflammatory cells and alleviate inflammation-mediated oxidative stress (Fig. 4H). The fluorescence signal intensity in inflammatory RAW 264.7 cells was observed by CLSM, which further verified that DSP@PS-Coac could be effectively internalized by cells and release drugs to alleviate inflammation-mediated oxidative stress *in vitro* (Fig. 4I). It was worth noting that the blank PS-Coac group also exhibited a certain antioxidant capacity. The possible reason might be the dual-enzyme activities of peroxidase and catalase inherent in ATP molecules, which could play a catalytic role in eliminating excessive ROS within cells and assist in maintaining cellular homeostasis[54].

3.5. *In vivo biodistribution behaviour of PS-Coac*

Subsequently, we further investigated the *in vivo* distribution behaviour of PS-Coac in ARDS model mice. Firstly, the ARDS model was induced in C57BL/6 male mice by tracheal drip infusion of LPS (5 mg/kg)[55]. We chose ICG, a hydrophilic fluorescent molecule with similar properties to the hydrophilic drug DSP, as the model fluorescent molecule. Free ICG, ICG@Coac and ICG@PS-Coac were injected *via* the tail vein 4 h after modelling. The major organs (heart, liver, spleen, lung and kidney) were taken from the mice at 1, 3, 6, 24 and 48 h after administration, respectively, and the *in vivo* biodistribution of the ARDS mice was examined by the *in vivo* imaging system (IVIS) in order to evaluate the lung-targeting ability of PS-Coac (Fig. 5A and B). The results showed that PS-lipo membranization increased the distribution level of fluorescent molecules in the lungs of ARDS mice and prolonged their lung retention time, as indicated by the results at different time points. After intravenous injection, free ICG molecules were mainly distributed in the liver and kidney, and only very weak fluorescent signals appeared in the lungs. The fluorescence of ICG further decreased after 3 h, indicating that the non-specifically distributed free ICG could be rapidly cleared from the body through the liver and kidney (Fig. 5C). At the same time points (1, 3, and 6 h), the lung fluorescence intensity of mice injected with ICG@Coac was stronger than that of the free ICG group. However, the fluorescence signals of the Coac group also diminished rapidly after 6 h. This may be due to the instability of the uncoated Coac, which gradually fused and partially depolymerized to release ICG molecules within 3 h. In contrast, the lung fluorescence signal in the well-stabilized ICG@PS-Coac group continuously increased within 24 h, and the lung-to-liver ratio gradually rose to a relatively high level. The further semi-quantitative analysis of the fluorescence signal intensity was shown in Fig. 5D−F and Supporting Information Fig. S18. After 24 h of administration, compared with the free ICG group, the lung distribution of ICG@PS-Coac increased to 60.5 times (free ICG: 0.16 *vs* ICG@PS-Coac: 9.67), and the lung-to-liver ratio increased to 42.3 times (free ICG: 0.09 *vs* ICG@PS-Coac: 3.68). Meanwhile, compared with free ICG, which was rapidly cleared within 6 h, the ICG@PS-Coac group still retained a relatively strong lung fluorescence signal (2.42) at 48 h, which indicated that PS-Coac has a good potential to prolong the lung retention time of the drug. The high distribution of PS-Coac in the lungs might be mainly attributed to the passive targeting effect mediated by the micron-sized dimension of PS-Coac. In addition, the lung-targeting properties of PS-based liposomes[56], the increased vascular permeability at the site of inflammation[57,58], and the increased endocytosis by AMs and ATIIs at the site of inflammation mediated by endogenous SP-A/D in alveoli[27,32] might also contribute to the enrichment of PS-Coac in inflamed tissues. Furthermore, the PEGylated phospholipids and the soft droplet characteristics of PS-Coac similar to neutrophils might also further promote the distribution of PS-Coac in the lungs. From the results, the PS-lipo membrane coating also effectively reduced the distribution in non-target organs (such as the liver and kidney), which was beneficial for reducing the toxic and side effects of the drug on non-target organs and improving the drug utilization rate.

In addition, we further verified the distribution of PS-Coac in the lungs of ARDS mice by immunofluorescence sections. Free FITC and FITC@PS-Coac were intravenously injected into ARDS mice through the tail vein, and lung tissue was collected and analyzed for fluorescence distribution by tissue immunofluorescence sectioning. The nuclei of the cells were labeled with DAPI (blue) (Fig. 5G). The results showed that no obvious fluorescent signals were seen for free FITC, while FITC@PS-Coac had a clear distribution inside the alveoli and surrounding tissues at 3, 6 and 24 h after injection, which demonstrated that PS-Coac was efficiently enriched in the inflamed lungs.

Previous studies have confirmed that anionic liposomes composed of the main phospholipid components of PS could target AMs and ATIIs by interacting with endogenous surfactant proteins. We hypothesized that AMs and ATIIs might be the target cells of PS-Coac[27,31,38]. Therefore, we further analyzed the cellular uptake of FITC@PS-Coac in lung tissues 24 h after intravenous injection through immunofluorescence sections. The results showed that in ARDS mice, FITC@PS-Coac could co-

Figure 5 *In vivo* distribution of PS-Coac. (A) Schematic diagram of the experimental steps for the *in vivo* distribution of PS-Coac. (B) Schematic diagram of the order of placement of the organs. (C) IVIS fluorescence images of major organs in mice after administration of free ICG, ICG@Coac and ICG@PS-Coac for different time points (1, 3, 6, 24 and 48 h) ($n = 4$). Fluorescence semi-quantitative analysis of (D) lungs, (E) livers and (F) lung/liver ratio ($n = 4$). (G) Fluorescence signals in lung tissues at 3, 6 and 24 h after injection of free FITC and FITC@PS-Coac (blue: DAPI; green: FITC@PS-Coac). Scale bar = 50 μm. Data are expressed as mean ± SD ($n = 3$); ***$P < 0.001$.

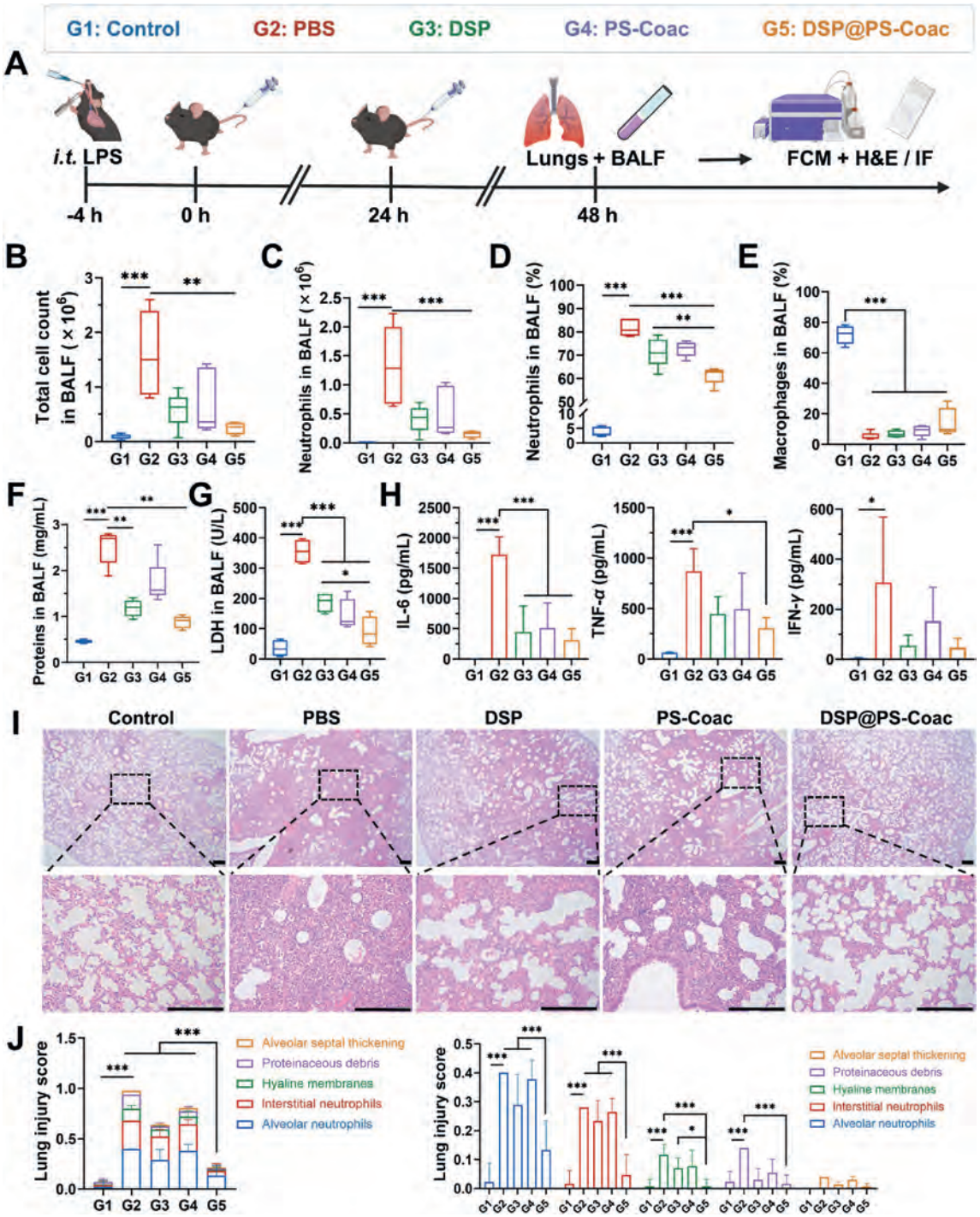

Figure 6 *In vivo* therapeutic efficacy of DSP@PS-Coac in LPS-induced ARDS mice. (A) Schematic of the treatment protocol in ARDS mice. (B) Total cell count and (C) neutrophil count in BALF of mice after treatments ($n = 5$). The proportion of (D) neutrophils and (E) macrophages in BALF ($n = 5$). (F) Protein content in BALF of mice after treatments ($n = 5$). (G) LDH concentration in BALF (U/L; $n = 5$). (H) Levels of major cytokines (IL-6, TNF-α, IFN-γ) in BALF ($n = 4$). (I) H&E-stained images of lung tissue sections. Scale bar = 200 μm. (J) Lung injury scores were obtained based on 5 pathophysiological features of H&E-stained images ($n = 3$). LPS stimulation was used in all groups except the Control group. Data are expressed as mean ± SD. $^*P < 0.05$, $^{**}P < 0.01$, $^{***}P < 0.001$.

localize with AMs (marked by CD68) and alveolar epithelial cells (marked by CK19) (Supporting Information Fig. S19, left and middle). In addition, given that neutrophils are also important primary phagocytic cells in the immune system, we also investigated the co-localization of FITC@PS-Coac with neutrophils in lung tissues. Notably, we found that neutrophils (marked by Ly6G) could also partially uptake FITC@PS-Coac (Fig. S18, right). In conclusion, these results suggest that after reaching the

lungs, PS-Coac might be effectively taken up by AMs, alveolar epithelial cells and neutrophils, and can effectively deliver the DSP into the cells and exert its therapeutic effect.

3.6. In vivo anti-inflammatory effects of PS-Coac in LPS-induced ARDS mice

To verify the therapeutic effects of PS-Coac, we investigated the *in vivo* anti-inflammatory effect in ARDS model mice. Briefly, an ARDS model was established in male C57 mice by intratracheal instillation of LPS at a dose of 5 mg/kg. Phosphate-buffered saline (PBS), free DSP, PS-Coac, and DSP@PS-Coac were intravenously injected 4 and 24 h later, respectively, with healthy mice serving as the positive control group. Bronchoalveolar lavage fluid (BALF) and lung tissues were collected at 24 h after the second administration for the analysis of inflammatory indicators (Fig. 6A). During the progression of ARDS, as first-response immune cells, neutrophils play an important driving role in the inflammatory response and are recruited in large numbers to the lungs in response to inflammatory signals. Therefore, we first evaluated the inflammatory regulation function of DSP@PS-Coac on ARDS mice by analyzing the inflammatory cells in BALF. As shown in Fig. 6B and C, only a small number of cells were found in the BALF of healthy mice. After LPS induction, both the total number of cells and the number of neutrophils in BALF were significantly increased. However, after treatment with DSP@PS-Coac, both the total number of cells and the total number of neutrophils were effectively decreased, which was the most obvious effect compared to the other treatment groups. Subsequently, we further evaluated the proportion of neutrophils and macrophages in BALF by FCM (Supporting Information Fig. S20). The results showed that the proportion of neutrophils in BALF increased obviously (about 80%) after LPS stimulation, whereas the proportion of neutrophils decreased to about 60% after DSP@PS-Coac treatment. The above results indicated that DSP@PS-Coac possessed good efficacy in inhibiting neutrophil infiltration (Fig. 6D and Supporting Information Fig. S21). However, there was no significant difference in the proportion of macrophages in BALF among the mice in each treatment group compared with that in the LPS group, suggesting that neutrophil infiltration was more evident during the acute exudative phase of ARDS (Fig. 6E). Nevertheless, there was no significant change in the body weight of mice among the different treatment groups during the treatment process of ARDS, indicating that the effect of drug treatment groups on restoring the body weight of mice was limited (Supporting Information Fig. S22).

The inflammatory response increases the permeability of the alveolar-capillary barrier, leading to the leakage of large amounts of protein-rich fluid into the alveolar and vascular spaces. Therefore, we measured the protein concentration in BALF to investigate the repair function of DSP@PS-Coac on the alveolar-capillary barrier. As shown in Fig. 6F, DSP@PS-Coac treatment effectively reduced the total protein concentration in BALF, indicating that the pulmonary vascular leakage was improved. In addition, we also detected the lactate dehydrogenase (LDH) concentration in BALF by an LDH assay kit. The results showed that LPS induction significantly increased the release of LDH, while DSP@PS-Coac treatment effectively reduced the LDH concentration in BALF, which suggested that DSP@PS-Coac could inhibit LPS-induced pulmonary cell damage and enhance cell viability (Fig. 6G). To further study the regulatory effect of DSP@PS-Coac on the pulmonary inflammatory microenvironment, we used a cytometric beads array (CBA) mouse inflammation kit to further detect the pro-inflammatory cytokines in the BALF of mice. As shown in Fig. 6H, DSP@PS-Coac treatment effectively reduced the levels of pro-inflammatory cytokines such as interleukin-6 (IL-6), tumor necrosis factor-α (TNF-α), and interferon-γ (IFN-γ) in BALF, demonstrating its ability to inhibit cytokine storm. Furthermore, the lung tissues after different drug treatments were isolated and examined by hematoxylin and eosin (H&E) staining to investigate the pulmonary pathological morphology of each group. The results showed that after LPS stimulation, the lung tissue exhibited obvious damage characterized by neutrophil infiltration, thickening of the alveolar septum, and vascular congestion, etc. DSP@PS-Coac treatment could reduce the pathological damage of the lung tissue, showing a significant decrease in neutrophil infiltration in the alveoli and pulmonary interstitium and a significant reduction in the lung parenchyma degree (Fig. 6I). Through further lung injury scoring, it was found that the score of the DSP@PS-Coac treatment group was obviously lower than that of the other groups, indicating that it could effectively relieve lung injury *in vivo* and promote the recovery of the structure and function of the lung tissue (Fig. 6J). Notably, the blank PS-Coac also showed a certain therapeutic effect in various indexes, which might be due to the immunomodulatory effect of the PS component itself, consistent with the reported results[56]. In summary, DSP@PS-Coac can effectively reduce pulmonary inflammatory damage in ARDS mice by inhibiting neutrophil infiltration, improving pulmonary vascular leakage, alleviating pulmonary cell damage and pathological damage, and suppressing the pro-inflammatory cytokine storm.

Subsequently, we further analyzed the immunomodulatory effect mediated by DSP@PS-Coac through immunofluorescence staining of lung tissues. Macrophages can be classified into M1 pro-inflammatory phenotype and M2 anti-inflammatory phenotype. M1 macrophages secrete multiple inflammatory mediators such as inducible nitric oxide synthase (iNOS), ROS, and nitric oxide (NO), which promote inflammation development and induce tissue damage. M2 macrophages secrete anti-inflammatory factors, upregulate arginase-1 (Arg-1), reduce NO and ROS levels, and promote inflammation resolution and repair of damaged tissues[59,60]. Driving the transformation of M1 inflammatory macrophages to the anti-inflammatory phenotype plays an important role in the treatment of ARDS. Therefore, we used macrophage-specific markers (M1: iNOS and M2: Arg-1) for immunofluorescence staining to investigate the polarization level of pulmonary macrophages in each treatment group. As shown in Fig. 7A and Supporting Information Fig. S23, under the stimulation of LPS, the level of iNOS in macrophages within the lung tissues of ARDS mice was significantly increased. After treatment with DSP@PS-Coac, iNOS expression was effectively decreased, while the level of Arg-1 was effectively upregulated. Compared with the other treatment groups, its effect on the polarization of macrophages to the M2 phenotype was more pronounced, which might be due to the fact that PS-Coac can more effectively deliver drugs to the inflamed lungs, and it also suggested a certain combined therapeutic effect of PS-Coac and DSP.

During the pathological process of ARDS, inflammatory cells can generate a large amount of ROS through oxidative stress reactions, causing varying degrees of damage to the structure and function of cells. We investigated the levels of ROS in lung tissues by means of immunofluorescence sections. As depicted in Fig. 7B, ROS levels in lung tissues of ARDS mice were significantly elevated after LPS stimulation. After DSP@PS-Coac treatment, the levels of ROS within the tissues were obviously

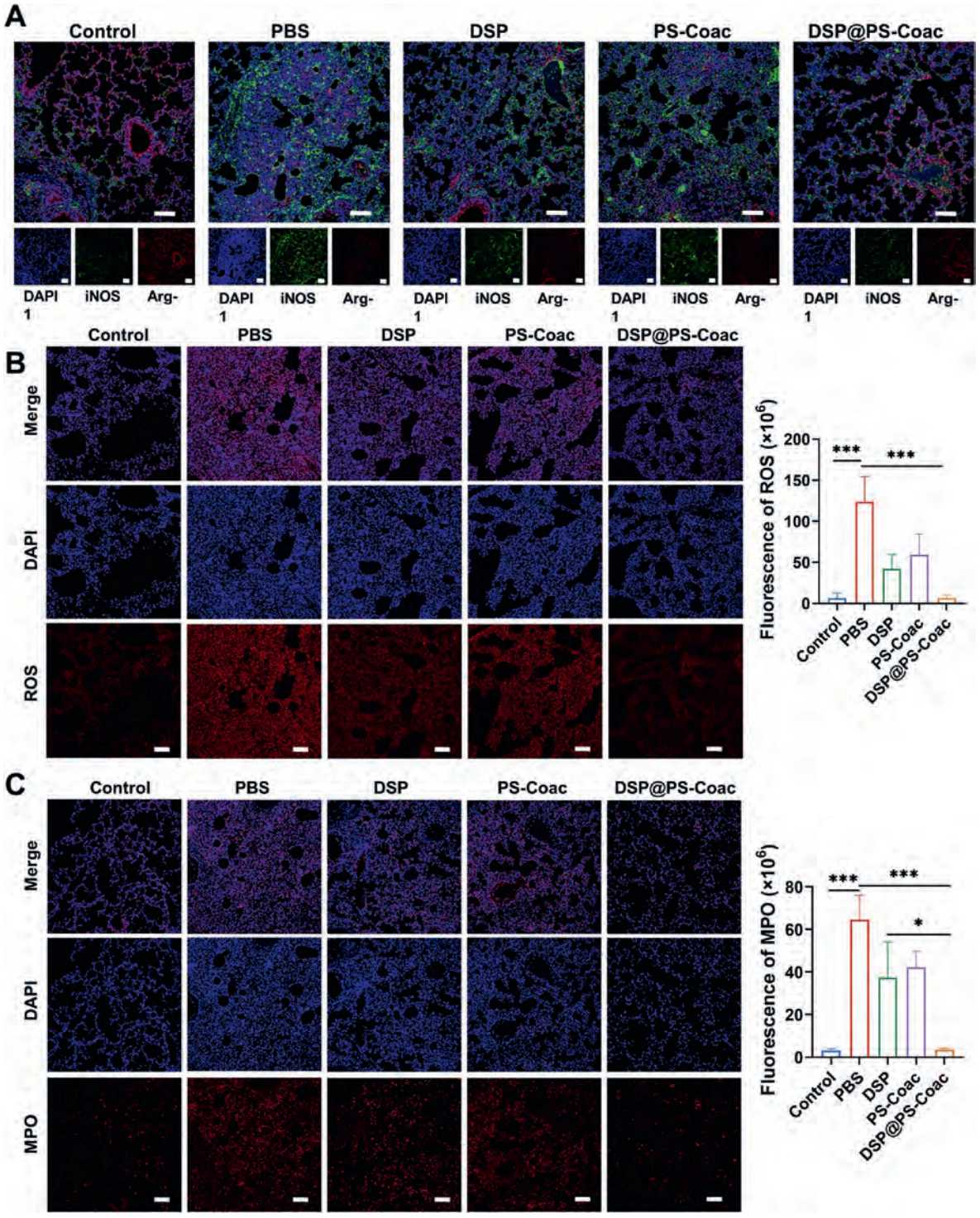

Figure 7 Immunofluorescence analysis of lung tissues in ARDS treated with DSP@PS-Coac. (A) Phenotypic analysis of macrophages in lung tissue. iNOS and Arg-1 were used as M1 and M2 macrophage markers, respectively. Immunofluorescence and semi-quantitative analysis of (B) ROS and (C) MPO in lung tissues. LPS stimulation was used in all groups except the Control group. Scale bar = 100 μm. Data are expressed as mean ± SD ($n = 3$); $^{*}P < 0.05$, $^{***}P < 0.001$.

decreased, suggesting that DSP@PS-Coac had the effect of alleviating oxidative stress damage caused by pulmonary inflammation, and this effect was more pronounced compared to that of free DSP. The possible reason might be that the ATP molecules inside PS-Coac play certain antioxidant functions as well as functions for replenishing the energy of damaged cells. Moreover, the excessive recruitment of pulmonary neutrophils during inflammation can lead to a large secretion of myeloperoxidase (MPO)[61]. Therefore, we also detected the content of MPO in the lung tissues of mice in each treatment group. As

shown by the fluorescence intensity, compared with normal mice, the content of MPO in the lung tissues of ARDS mice was effectively increased. Treatment with either DSP or PS-Coac alone could moderately inhibit the excessive production of ROS in the lung tissues. DSP@PS-Coac exhibited a stronger inhibition on the secretion of MPO compared to free DSP and PS-Coac, which might be related to its effect of reducing the recruitment of neutrophils (Fig. 7C).

4. Conclusions

A pulmonary surfactant-biomimetic membranized coacervate (PS-Coac) was developed as a pulmonary drug delivery carrier. Benefiting from the lung-targeting performance and prolonged lung retention time of PS-Coac, DSP@PS-Coac demonstrated favorable therapeutic effects in the ARDS model. Our study holds certain potential in the treatment of ARDS as well as other acute and chronic pulmonary diseases. Nevertheless, limited by the current technological capabilities, our research could be further improved through the following approaches. Firstly, based on the chemical structure of PAH (rich in primary amine groups), we preliminarily speculate that PAH might be mainly excreted from the body in its original form through the kidneys and the liver[62]. But there is still a severe shortage of research on the specific *in vivo* metabolic pathway, degradation kinetic, and long-term toxicity of PAH, which remains to be further investigated in the subsequent studies. Secondly, given the excellent potential of PS-Coac for co-loading macromolecules and small molecules as well as hydrophilic and hydrophobic molecules, along with the drug treatment challenges faced by ARDS in clinical practice, effective drug co-delivery formulations could be further designed to enhance its clinical therapeutic potential. Finally, the in-depth study of the carrier's *in vivo* therapeutic mechanism will be conducive to its further progress towards clinical research[63]. Therefore, the *in vivo* anti-inflammatory mechanism of DSP@PS-Coac could be further investigated, and then the carrier design protocol could be improved in a targeted manner to enhance its therapeutic efficacy for ARDS.

Acknowledgments

This work was supported by the National Natural Science Foundation of China (Nos. 8237131246 and 32271454), the Program for HUST Academic Frontier Youth Team (2018QYTD13), Wuhan Science and Technology Plan (2022023702025187, China), and Natural Science Foundation of Hubei Province (2024AFB582, China). We thank Ms. Sisi Li from the Analytical and Testing Center of Huazhong University of Science & Technology (HUST) for her technical support on TEM. We thank the Laboratory Animal Center of HUST for the raising and care of animals.

Author contributions

Wei Chen: investigation, methodology, data curation, formal analysis, conceptualization, writing-original draft. Qi Xie: investigation, visualization, methodology, writing-original draft. Zhanhao Zhou: methodology, writing-original draft. Jia Kang: data curation. Yuan Gao: data curation. Haoyu Zhang: methodology. Samira Batur: methodology. Chuansheng Fu: methodology. Yunyun Li: methodology. Conglian Yang: supervision. Li Kong: writing−review & editing, supervision. Zhiping Zhang: supervision, writing−review & editing, conceptualization. All authors read and approved the final manuscript.

Conflicts of interest

There are no conflicts of interest to declare.

Appendix A. Supporting information

Supporting information to this article can be found online at https://doi.org/10.1016/j.apsb.2025.08.025.

References

1. Dushianthan A, Grocott MP, Postle AD, Cusack R. Acute respiratory distress syndrome and acute lung injury. *Postgrad Med J* 2011;**87**:612−22.
2. Bos LDJ, Ware LB. Acute respiratory distress syndrome: causes, pathophysiology, and phenotypes. *Lancet* 2022;**400**:1145−56.
3. Bellani G, Laffey JG, Pham T, Fan E, Brochard L, Esteban A, et al. Epidemiology, patterns of care, and mortality for patients with acute respiratory distress syndrome in intensive care units in 50 countries. *JAMA* 2016;**315**:788−800.
4. Kim HA, Park JH, Lee S, Choi JS, Rhim T, Lee M. Combined delivery of dexamethasone and plasmid DNA in an animal model of LPS-induced acute lung injury. *J Control Release* 2011;**156**:60−9.
5. Tang W, Zhao ZB, Chong YY, Wu CF, Liu QZ, Yang JB, et al. Tandem enzymatic self-assembly and slow release of dexamethasone enhances its antihepatic fibrosis effect. *ACS Nano* 2018;**12**:9966−73.
6. Wang XQ, Zhou X, Zhou Y, Rong L, Gao L, Xu W. Low-dose dexamethasone alleviates lipopolysaccharide-induced acute lung injury in rats and upregulates pulmonary glucocorticoid receptors. *Respirology* 2008;**13**:772−80.
7. Qiao Q, Liu X, Yang T, Cui KX, Kong L, Yang CL, et al. Nanomedicine for acute respiratory distress syndrome: the latest application, targeting strategy, and rational design. *Acta Pharm Sin B* 2021;**11**:3060−91.
8. García-Fernández A, Sancho M, Bisbal V, Amorós P, Marcos MD, Orzáez M, et al. Targeted-lung delivery of dexamethasone using gated mesoporous silica nanoparticles. A new therapeutic approach for acute lung injury treatment. *J Control Release* 2021;**337**:14−26.
9. Muhammad W, Zhu JQ, Zhai ZH, Xie JQ, Zhou JH, Feng XD, et al. ROS-responsive polymer nanoparticles with enhanced loading of dexamethasone effectively modulate the lung injury microenvironment. *Acta Biomater* 2022;**148**:258−70.
10. Zhai ZH, Ouyang W, Yao YJ, Zhang YQ, Zhang HL, Xu F, et al. Dexamethasone-loaded ROS-responsive poly(thioketal) nanoparticles suppress inflammation and oxidative stress of acute lung injury. *Bioact Mater* 2022;**14**:430−42.
11. Meyer NJ, Gattinoni L, Calfee CS. Acute respiratory distress syndrome. *Lancet* 2021;**398**:622−37.
12. Aumiller Jr WM, Pir Cakmak F, Davis BW, Keating CD. RNA-based coacervates as a model for membraneless organelles: formation, properties, and interfacial liposome assembly. *Langmuir* 2016;**32**:10042−53.
13. Gaur D, Dubey NC, Tripathi BP. Biocatalytic self-assembled synthetic vesicles and coacervates: from single compartment to artificial cells. *Adv Colloid Interface Sci* 2022;**299**:102566.
14. Ji YLM, Lin YY, Qiao Y. Plant cell-inspired membranization of coacervate protocells with a structured polysaccharide layer. *J Am Chem Soc* 2023;**145**:12576−85.
15. Xu C, Martin N, Li M, Mann S. Living material assembly of bacteriogenic protocells. *Nature* 2022;**609**:1029−37.
16. Uversky VN. Protein intrinsic disorder-based liquid−liquid phase transitions in biological systems: complex coacervates and membraneless organelles. *Adv Colloid Interface Sci* 2017;**239**:97−114.

17. Dolgin E. What lava lamps and vinaigrette can teach us about cell biology. *Nature* 2018;**555**:300−2.
18. Wen P, Huang HW, Zhang RZ, Zheng HQ, Liang TXZ, Zhuang CY, et al. Coacervate vesicles assembled by liquid−liquid phase separation improve delivery of biopharmaceuticals. *Nat Chem* 2025;**17**:279−88.
19. Liang TXZ, Dong YX, Cheng I, Wen P, Li FQ, Liu F, et al. *In situ* formation of biomolecular condensates as intracellular drug reservoirs for augmenting chemotherapy. *Nat Biomed Eng* 2024;**8**:1469−82.
20. Liu J, Zhorabek F, Zhang T, Lam JWY, Tang BZ, Chau Y. Multifaceted cargo recruitment and release from artificial membraneless organelles. *Small* 2022;**18**:e2201721.
21. Blocher McTigue WC, Perry SL. Protein encapsulation using complex coacervates: what nature has to teach us. *Small* 2020;**16**:e1907671.
22. Sun Y, Lau SY, Lim ZW, Chang SC, Ghadessy F, Partridge A, et al. Phase-separating peptides for direct cytosolic delivery and redox-activated release of macromolecular therapeutics. *Nat Chem* 2022;**14**:274−83.
23. Paganini C, Capasso Palmiero U, Picciotto S, Molinelli A, Porello I, Adamo G, et al. High-yield separation of extracellular vesicles using programmable zwitterionic coacervates. *Small* 2023;**19**:e2204736.
24. Hu Q, Lan HB, Tian YM, Li XN, Wang MM, Zhang J, et al. Biofunctional coacervate-based artificial protocells with membrane-like and cytoplasm-like structures for the treatment of persistent hyperuricemia. *J Control Release* 2024;**365**:176−92.
25. Parra E, Pérez-Gil J. Composition, structure and mechanical properties define performance of pulmonary surfactant membranes and films. *Chem Phys Lipids* 2015;**185**:153−75.
26. Holm BA, Wang Z, Notter RH. Multiple mechanisms of lung surfactant inhibition. *Pediatr Res* 1999;**46**:85−93.
27. Herman L, De Smedt SC, Raemdonck K. Pulmonary surfactant as a versatile biomaterial to fight COVID-19. *J Control Release* 2022;**342**:170−88.
28. Polin RA, Carlo WA. Surfactant replacement therapy for preterm and term neonates with respiratory distress. *Pediatrics* 2014;**133**:156−63.
29. Sweet DG, Carnielli VP, Greisen G, Hallman M, Klebermass-Schrehof K, Ozek E, et al. European consensus guidelines on the management of respiratory distress syndrome: 2022 update. *Neonatology* 2023;**120**:3−23.
30. Chroneos ZC, Sever-Chroneos Z, Shepherd VL. Pulmonary surfactant: an immunological perspective. *Cell Physiol Biochem* 2010;**25**:13−26.
31. Wang BH, Gao YW, Sun LL, Xue M, Wang MJ, Zhang ZZ, et al. Inhaled pulmonary surfactant biomimetic liposomes for reversing idiopathic pulmonary fibrosis through synergistic therapeutic strategy. *Biomaterials* 2023;**303**:122404.
32. Rao L, Zhu PJ, Guo MY, Hu MD, Guo XC, Du YZ, et al. Nebulized inhalation of nintedanib-loaded biomimetic nano-liposomes attenuated bleomycin-induced interstitial lung fibrosis in mice. *Nano Today* 2024;**56**:102298.
33. Veldhuizen RAW, Zuo YY, Petersen NO, Lewis JF, Possmayer F. The COVID-19 pandemic: a target for surfactant therapy?. *Expet Rev Respir Med* 2021;**15**:597−608.
34. Hidalgo A, Cruz A, Pérez-Gil J. Barrier or carrier? Pulmonary surfactant and drug delivery. *Eur J Pharm Biopharm* 2015;**95**:117−27.
35. Wright JR. Clearance and recycling of pulmonary surfactant. *Am J Physiol* 1990;**259**:L1−12.
36. Andreeva AV, Kutuzov MA, Voyno-Yasenetskaya TA. Regulation of surfactant secretion in alveolar type II cells. *Am J Physiol Lung Cell Mol Physiol* 2007;**293**:L259−71.
37. Hidalgo A, Cruz A, Pérez-Gil J. Pulmonary surfactant and nanocarriers: toxicity versus combined nanomedical applications. *Biochim Biophys Acta Biomembr* 2017;**1859**:1740−8.
38. Wang J, Li PY, Yu Y, Fu YH, Jiang HY, Lu M, et al. Pulmonary surfactant-biomimetic nanoparticles potentiate heterosubtypic influenza immunity. *Science* 2020;**367**:eaau0810.
39. Jiang JL, Cui XY, Huang YX, Yan DM, Wang BS, Yang ZY, et al. Advances and prospects in integrated nano-oncology. *Nano Biomed Eng* 2024;**16**:152−87.
40. Sarwar MS, Ghaffar A, Huang Q, Khalid M, Anwar A, Alayoubi AM, et al. Controlled drug release contenders comprising starch/poly (allylamine hydrochloride) biodegradable composite films. *Int J Biol Macromol* 2023;**241**:124598.
41. Zhang RR, Li RF, Zhang L, Chen G, Mo LF, Jiang R, et al. A dual-mechanism based nutrient partitioning nanoregulator for enhanced immunotherapy against anti-PD-1 resistant tumors. *ACS Nano* 2023;**17**:13461−73.
42. Janeesh PA, Sami H, Dhanya CR, Sivakumar S, Abraham A. Biocompatibility and genotoxicity studies of polyallylamine hydrochloride nanocapsules in rats. *RSC Adv* 2014;**4**:24484−97.
43. Fu FS, Chen HH, Chen Y, Yuan Y, Zhao Y, Yu A, et al. Engineered bacillus subtilis enhances bone regeneration *via* immunoregulation and anti-infection. *Bioact Mater* 2025;**46**:503−15.
44. Qin YT, Rao ZY, An JX, Zhang SM, Wang YZ, Pan T, et al. Inhibiting chemotherapy immune tolerance and reversing tumor microenvironment by macrophage-targeted nanohybrid systems for enhancing tumor chemo-immunotherapy. *Adv Funct Mater* 2025;**35**:2501954.
45. Pir Cakmak F, Grigas AT, Keating CD. Lipid vesicle-coated complex coacervates. *Langmuir* 2019;**35**:7830−40.
46. Zhou ZH, Lan HB, Tan HY, Wang Y, Chen W, Batur S, et al. ROS-responsive biomimetic nanovesicles to plaque microenvironment in targeted therapy of atherosclerosis. *Nano Today* 2024;**59**:102530.
47. Cao S, Ivanov T, Heuer J, Ferguson CTJ, Landfester K, Caire da Silva L. Dipeptide coacervates as artificial membraneless organelles for bioorthogonal catalysis. *Nat Commun* 2024;**15**:39.
48. Yin CY, Lin Z, Jiang XY, Martin N, Tian LF. Engineering the coacervate microdroplet interface *via* polyelectrolyte and surfactant complexation. *ACS Appl Mater Interfaces* 2023;**15**:27447−56.
49. Lu T, Spruijt E. Multiphase complex coacervate droplets. *J Am Chem Soc* 2020;**142**:2905−14.
50. Donau C, Späth F, Sosson M, Kriebisch BAK, Schnitter F, Tena-Solsona M, et al. Active coacervate droplets as a model for membraneless organelles and protocells. *Nat Commun* 2020;**11**:5167.
51. Gao N, Mann S. Membranized coacervate microdroplets: from versatile protocell models to cytomimetic materials. *Acc Chem Res* 2023;**56**:297−307.
52. Gong XT, Chong KC, Liu J, Cheng W, Yang J, Liu B. AIENP-reinforced DISCO method for whole-tissue 3D reconstruction of pulmonary capillaries. *Adv Funct Mater* 2024;**34**:2312176.
53. Liu HY, Du L, Zhao YT, Tian WQ. *In vitro* hemocompatibility and cytotoxicity evaluation of halloysite nanotubes for biomedical application. *J Nanomater* 2015;**2015**:1−9.
54. Shi Y, Tang MH, Sun CQ, Pan YD, Liu L, Long YJ, et al. ATP mimics pH-dependent dual peroxidase-catalase activities driving H_2O_2 decomposition. *CCS Chem* 2019;**1**:373−83.
55. Qiao Q, Liu X, Cui KX, Li XN, Tian TY, Yu YL, et al. Hybrid biomimetic nanovesicles to drive high lung biodistribution and prevent cytokine storm for ARDS treatment. *ACS Nano* 2022;**16**:15124−40.
56. Arber Raviv S, Alyan M, Egorov E, Zano A, Harush MY, Pieters C, et al. Lung targeted liposomes for treating ARDS. *J Control Release* 2022;**346**:421−33.
57. Igarashi K, Cabral H, Hong T, Anraku Y, Mpekris F, Stylianopoulos T, et al. Vascular bursts act as a versatile tumor vessel permeation route for blood-borne particles and cells. *Small* 2021;**17**:e2103751.
58. Ibaraki H, Takeda A, Arima N, Hatakeyama N, Takashima Y, Seta Y, et al. *In vivo* fluorescence imaging of passive inflammation site accumulation of liposomes *via* intravenous administration focused on their surface charge and PEG modification. *Pharmaceutics* 2021;**13**:104.

59. Aggarwal NR, King LS, D'Alessio FR. Diverse macrophage populations mediate acute lung inflammation and resolution. *Am J Physiol Lung Cell Mol Physiol* 2014;**306**:L709−25.
60. Hu Q, Lyon CJ, Fletcher JK, Tang W, Wan M, Hu TY. Extracellular vesicle activities regulating macrophage- and tissue-mediated injury and repair responses. *Acta Pharm Sin B* 2021;**11**:1493−512.
61. Liu X, Qiao Q, Li XN, Ou XJ, Cui KX, Niu BN, et al. Apoptotic neutrophil-mediated inflammatory microenvironment regulation for the treatment of ARDS. *Nano Today* 2023;**52**:101946.
62. Pottel H, Delanaye P, Cavalier E. Exploring renal function assessment: creatinine, cystatin C, and estimated glomerular filtration rate focused on the european kidney function consortium equation. *Ann Lab Med* 2024; **44**:135−43.
63. Li M, Lu LS, Xiao QG, Maalim AA, Nie B, Liu YC, et al. Bioengineer mesenchymal stem cell for treatment of glioma by IL-12 mediated microenvironment reprogramming and nCD47-SLAMF7 mediated phagocytosis regulation of macrophages. *Explorations* 2024;**4**: 20240027.